The potential of using a three-port Mach-Zehnder interferometer for biosensing and displacement sensing

R.J.J. van Gulik

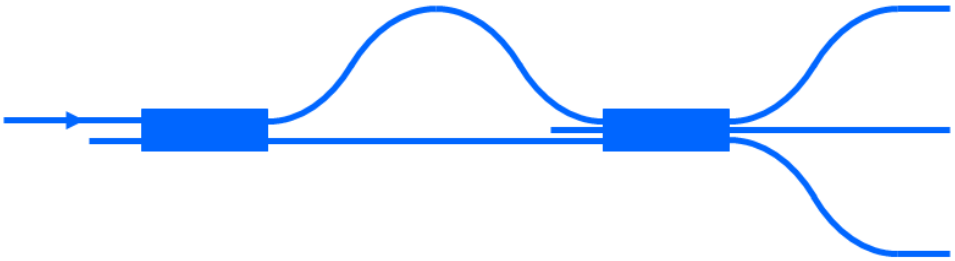

Company supervisor:
P.J. Harmsma

Educational supervisor:
R. Buning

TNO, Delft
De Haagse Hogeschool Delft
June 2, 2016

Abstract

Integrated photonic sensors are promising devices for various sensing applications due to their low cost, small size, and high sensitivities that can be reached. In this thesis, ring resonators and three-port Mach-Zehnder interferometer (MZI) devices fabricated on Silicon-On-Insulator were compared for the purpose of refractive index sensing. This can be used to make biosensors for use in a lab-on-a-chip or treatment at the point-of-care. Their respective sensitivities and limits of detection (LOD) were determined with NaCl solutions. A sensitivity of 113.07 nm per refractive index unit (RIU) and an LOD of $2.47 \cdot 10^{-6}$ RIU was reached for the ring resonators. The most sensitive three-port MZI has a sensitivity of 13 051 rad/RIU, and an LOD of $2.76 \cdot 10^{-8}$ RIU is shown to be attainable. A three-port MZI combines several advantages of both ring resonators and normal MZI devices, including a constant and scalable sensitivity, high-bandwidth readout, no directional ambiguity, and a simple interrogation setup. Such a device is promising for biosensing, but also other applications like ultrasound, pressure, and gas sensing.

In addition to that, a setup has been built to characterize a three-port MZI fabricated on InP for the purpose of displacement sensing. These sensors have applications in the active stabilization of objects that are required to be isolated from vibrations, such as in nanotechnology fabrication. A factor 20 reduction of noise caused by wavelength fluctuations was achieved compared to previous measurements. Further characterization in a vibration-isolated environment is necessary to attribute a detection limit to the device.

Contents

Abbreviations

ADC	Analog-to-Digital Converter
ER	Extinction Ratio
FFT	Fast Fourier Transform
FSR	Free Spectral Range
FWHM	Full Width at Half Maximum
LOD	Limit Of Detection
MMI	Multi Mode Interference
MZI	Mach-Zehnder Interferometer
OSA	Optical Spectrum Analyzer
PIC	Photonic Integrated Circuit
RIU	Refractive Index Units
SOI	Silicon-On-Insulator
TE	Transverse Electric
TIA	TransImpedance Amplifier
TIR	Total Internal Reflection
TLS	Tunable Laser Source
TM	Transverse Magnetic
VGC	Vertical Grating Coupler

Symbols

λ	Wavelength
t	Time
ω	Angular frequency
c	Speed of light in a vacuum

1 Introduction

Interferometry using light has been and still is a very important tool for measuring small variations in distance, owing to the wavelength of light commonly being in the nanometer range. Devices using this principle are called interferometers, with the first and most well-known example being the Michelson interferometer used in the Michelson-Morley experiment [1]. In this experiment the speed of light was measured to be constant in different reference frames, disproving the existence of a theorized 'luminiferous aether' in which light was thought to propagate. This null result eventually lead to the formulation of the theories of special [2] and later general relativity [3] by Einstein. Most recently this very same interferometry configuration has been used by the Laser Interferometer Gravitational-wave Observatory (LIGO) collaboration to detect and thus directly prove the existence of gravitational waves [4], confirming the predictions of Einstein's general relativity.

1.1 Photonic devices and technology

The invention of the laser in the 1960's was crucial to interferometric measurements due to its output being of long coherence length and high power. Soon after that low-loss optical fibers were developed for usage in communications [5], and together with the first semiconductor lasers the field of photonics emerged. Rapid advancements in semiconductor fabrication technology allowed for ever smaller integrated electronic circuits (ICs) on chips to be created. Eventually the dimensions became small enough for single-mode waveguides to be made to transport light around a chip in the same way that electrical signals are transported around an IC, such devices are called photonic integrated circuits (PICs). Most optical components at the time were fabricated from semiconductor materials as gallium arsenide (GaAs) and indium phosphide (InP). As lithography resolution increased further, the usage of the cheaper silicon (Si) as a waveguide material became possible with the required waveguide dimensions on the order of several hundred nanometers.

Following this, the development of components like on-chip light sources and lasers, detectors, splitters and multiplexers made Si and InP promising platforms for optical communication devices and sensors of which examples are shown in figure 1.1. The integration of on-chip light sources and detectors is more trivial in InP due to its direct bandgap opposed to the indirect bandgap of silicon. When active components are not needed, silicon offers the advantages of being low-cost and allowing tighter waveguide bends due to its high refractive index contrast (15 μm radius vs. 200 μm).

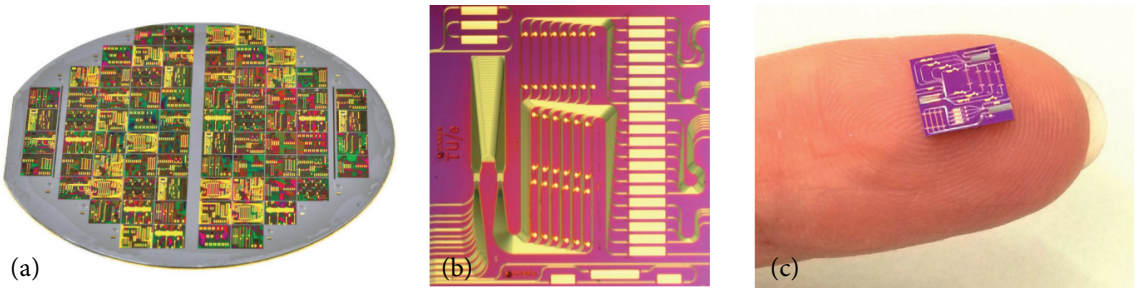

Figure 1.1: Images are taken from [6] (a) Example of a multi-project wafer containing PICs designed by multiple customers. (b) A photonic chip containing a pulse-shaping circuit for bio-imaging. (c) A photonic multi-channel transmitter for use in telecommunications.

Designing the individual components that are used in PICs and manufacturing them is a time-consuming and expensive process which is limiting companies in experimenting with this emerging technology. In the last years several initiatives have been started with the goal of providing standardized design procedures to promote and improve access to the use of photonics. These initiatives partner with existing semiconductor fabrication plants (foundries). The ePIXfab [7] alliance focuses primarily on Si as a platform and JePPIX on InP. An example of the methods they use are multi-project wafer runs in which multiple chip designs are fabricated on the same wafer in order to share the initial costs of creating the lithography mask amongst other things.

1.2 Biosensing

When concentrations of certain chemical substances like greenhouse gasses in the air or proteins and antibodies in the blood or urine of a person have to be measured, there is often need for specialized measurement equipment. In the case of blood a sample will have to be taken and sent to a lab to be processed there, and it usually takes a few days for the results to come back. Sometimes it is crucial that there is a fast analysis in order to treat the patient as soon as possible and prevent further worsening of a condition.

Since the advent of PICs there has been an interest in using them as so-called biosensors. There are several clear advantages when compared to traditional methods of analysis. Costs can be greatly reduced as mass-produced PICs cost only on the order of several cents per chip. Fully integrating the sensors as a lab-on-a-chip (LOC) environment and including automated measurement software can allow for non-specifically trained people like general practitioners to perform analysis in their own clinics, also called diagnostics at the point-of-care. This comes with improvements in the time and costs that normal measurements in a laboratory take. Over the past two decades multiple concepts for optical biosensors have been realized, usually based on the principle of an evanescent field interacting with the sample. As light travels through a waveguide, a fraction of it extends just outside the core, and changes in this medium will also affect the light. A short description of several types of optical biosensors will be given below, with their performance generally characterized by a minimum detectable change in refractive index units (RIU).

Biosensors based on a Mach-Zehnder interferometer (MZI) work by letting the substance of interest interact with the evanescent field of either one or both of the arms. The change in refractive index due to this substance results in a changing output intensity. Several groups have realized MZI-based biosensors, with limits of detection (LODs) on the order of 10^{-6} to 10^{-8} RIU [8–13]. While allowing for very low detection limits, there are two significant drawbacks. The sensitivity of the MZI will depend on the position in the fringe sinusoid, being almost zero at the extremes. In addition to that there is no clarity about whether the concentration is increasing or decreasing. A method for solving these problems is a modulation of the input power, compromising some of the simplicity of the MZI [9, 10, 14]. Three-port MZIs solve these problem and have been developed using directional couplers to create the 120° phase differences [15, 16], or using 3×3 Multi Mode Interference (MMI) couplers [17].

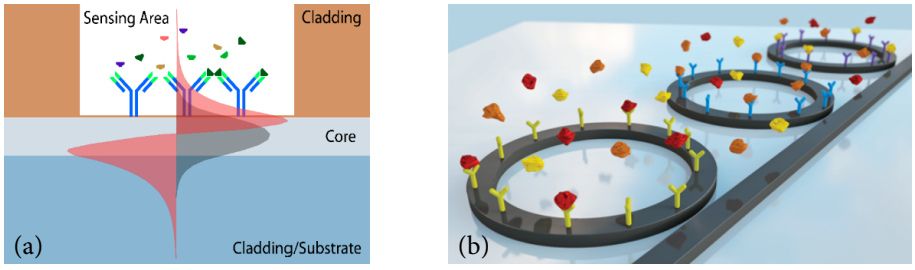

Figure 1.2: (a) The detection principle, the evanescent field in gray and red interacts with the receptor molecules on top of the waveguide core. (b) Impression of ring resonators with different receptor molecules.

Ring resonators act as a resonance cavity in the way that only light with a wavelength that fits an integer amount inside the ring can interfere constructively and build up in intensity. As the wavelength is determined by the refractive index, which in turn changes because of a substance flown over the chip surface, the resonant wavelengths will shift indicating a changing concentration. Various ring resonator based biosensors

have been realized, with detection limits down to 10^{-7} RIU [18–20]. While ring resonators have shown to be a promising biosensor platform, their read-out is complicated by the fact that it requires the wavelength to be scanned. With the resonance shift precision being dependent on the wavelength resolution, it calls for expensive tunable lasers. For several years now the Netherlands Organization for Applied Scientific Research (TNO) has been performing research on the use of silicon-on-insulator (SOI) based ring resonators as biosensors. They have worked on bringing down the instrumentation cost by proposing an on-chip tunable vertical cavity surface emitting laser (VCSEL) and a wavelength tracker based on a three-port MZI [21]. As a step in this direction, TNO has developed a portable setup called the FRESCO which can be used to perform analysis after about half an hour of training [22].

In this thesis, the three-port MZI that is available on existing chips developed by TNO with the original purpose of wavelength tracking for ring resonators is further explored for its use as refractive index sensor. Compared to ring resonators a three-port MZI offers the advantage of a sensitivity that is proportional to the arm length, allowing for very high sensitivities to be reached. In addition, the interrogation method is simple and requires only a constant wavelength source in contrast to an expensive tunable laser. Not being required to do wavelength sweeps, read-out bandwidths of tens of kHz are easily reached. Temperature influence is very low when both arms are made equal and does not require an additional reference sensor. When compared to regular MZI sensors the three-port MZI offers a nearly constant sensitivity at every point in a measurement and no directional ambiguity in changes of the refractive index. All these advantages make three-port MZIs very promising devices for biosensing and other applications like ultrasound, pressure, and gas sensing. The sensitivities of both the ring resonators and three-port MZIs are measured and detection limits are investigated to give advice on what factors are currently limiting the performance and which areas can be improved upon.

1.3 Displacement sensing

Interferometry is also a prime candidate for measuring displacement. One of the applications that displacement sensors can be used for is active isolation from vibrations in tables or objects that need to be stabilized. The need for extremely stable surfaces arises when working in the nanoscale such as in lithography or electron and atomic force microscopy. As the technology gets more advanced and the length scales go down, the effect of vibrations gets larger and must be reduced. Buildings where vibration-sensitive research is done often have large foundations or the equipment is placed on heavy objects to reduce high-frequency vibrations. After this effort, lower frequencies in the order of 1 Hz still remain and must be actively compensated for.

TNO has developed such a table called the 'Kolibri' for use in nanotechnology labs [23]. An interferometer senses the displacement of the table in various degrees of freedom and a control mechanism moves the table in the opposite direction to counteract the vibrations.

Utilizing a three-port MZI on a photonic chip could reduce the costs and volume of such a displacement sensor. In this thesis, the novel concept of an on-chip photonic displacement sensor is further explored to characterize the dominant noise sources and provide an outlook for improving the device.

2 Theory of integrated photonics and photonic sensing

In this chapter the underlying theory of integrated photonics and its components is discussed.

2.1 Waveguides

The simplest waveguide is the dielectric slab waveguide consisting of an inner layer called the core and surrounded on two sides by the outer cladding layers as seen in figure 2.1. The refractive index of the core n_1 is higher than that of the cladding n_2 so that total internal reflection (TIR) can occur provided that the angle of incidence θ_m is greater than the critical angle θ_c as defined by $\sin\theta_c = n_2/n_1$. Because the light reflects back and forth between the two cladding layers it effectively propagates forwards in a single direction.

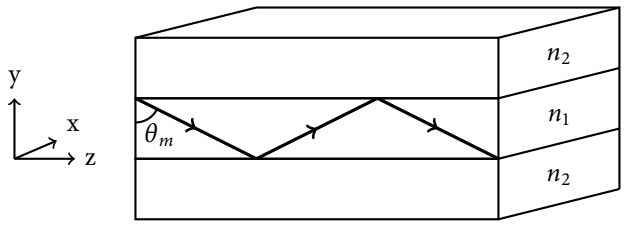

Figure 2.1: Schematic of a diëlectric slab waveguide.

However, not all light at angles $\theta_m > \theta_c$ can exist inside the waveguide as the phasefronts from different reflections of the electromagnetic (EM) wave have to match up or else destructive interference occurs. From a geometrical analysis considering both the angle of incidence and phase shift caused by reflection, which depends on the incidence angle according to the Fresnel equations, it can be shown that the condition

$$\left(\frac{2\pi n_1 d}{\lambda}\right)\cos\theta_m - \phi_m = m\pi \qquad \text{with} \qquad m = 1, 2, 3, \ldots \tag{2.1}$$

where

d	core slab thickness	(m)
θ_m	mode angle of incidence	(rad)
ϕ_m	phase shift by reflection	(rad)

must be satisfied. The different solutions for θ_m in formula 2.1 are called the modes or eigenmodes of the waveguide with m the mode number. There are a finite number of solutions to this equation for $\theta_c < \theta_m < 90°$. Each of these modes has a propagation constant $k = 2\pi/\lambda$ in both the upward and downward reflecting directions. Because considering both directions in a superposition gives a standing wave in the y-direction, the y-components of k cancel out resulting in an effective propagation constant of $\beta_m = k\sin\theta_m$ along the z-axis. Similarly, an effective refractive index can be assigned to each mode by the relation $n_{\text{eff}} = \beta_m/k_0$ where k_0 is the vacuum propagation constant $2\pi/\lambda_0$ and λ_0 the wavelength in a vacuum. This n_{eff} however only gives information about the speed with which the phase fronts propagate, the phase velocity v_{ph}. Because of

chromatic dispersion caused by the wavelength dependence of the refractive index of a material, the actual information or energy propagates at the group velocity v_g with corresponding group refractive index

$$n_g = n_{\text{eff}} - \lambda \frac{dn_{\text{eff}}}{d\lambda}. \tag{2.2}$$

This standing wave can be seen as an electric field distribution along the y-axis propagating in the z-direction and winding in phase according to [24]

$$E(y,z,t) = E_m(y)\cos(\omega t - \beta_m z) \tag{2.3}$$

where

E	resulting electric field	(V/m)
E_m	electric field distribution	(V/m)
β_m	mode propagation constant	(rad/m).

The fact that modes of a waveguide propagate at different speeds introduces another kind of dispersion called modal dispersion [24]. When a short pulse is supplied to a waveguide the output pulse will appear broadened due to the modes arriving at different times. To prevent this the dimensions of the core of the waveguide can be chosen so that below a certain cutoff wavelength there can only exist one mode, eliminating modal dispersion. Such a waveguide is called single-mode.

The electric field of light that propagates in a waveguide such as that in figure 2.1 can be divided into a component perpendicular and parallel to the core-cladding boundary. Because these two components experience a different phase shift according to the Fresnel equations for reflection, they will result in a slightly different mode and propagation constants by equation 2.1. These modes are either called transverse electric (TE) for an electric field perpendicular to the boundary and transverse magnetic (TM) for the field parallel to it.

The slab waveguide is a good theoretical model but since it uses planes of infinite extent it is not very useful in practice. In reality, waveguides are usually in the form of a strip waveguide in the case of PICs, or in the form of optical fibers for telecommunications. Silicon is a good waveguide core material because of its high refractive index (3.45) compared to materials as SiO_2 (1.5) and air (1.0) that are used as cladding. SOI waveguides are fabricated by thermally oxidizing a layer of SiO_2 on top of a Si substrate and etching away what is not part of the waveguide. A commonly used dimension for SOI waveguides is 450 nm wide and 220 nm thick so it is single-mode for both TE and TM polarized light at around 1550 nm [7]. The mode profiles of both modes are shown in figure 2.2.

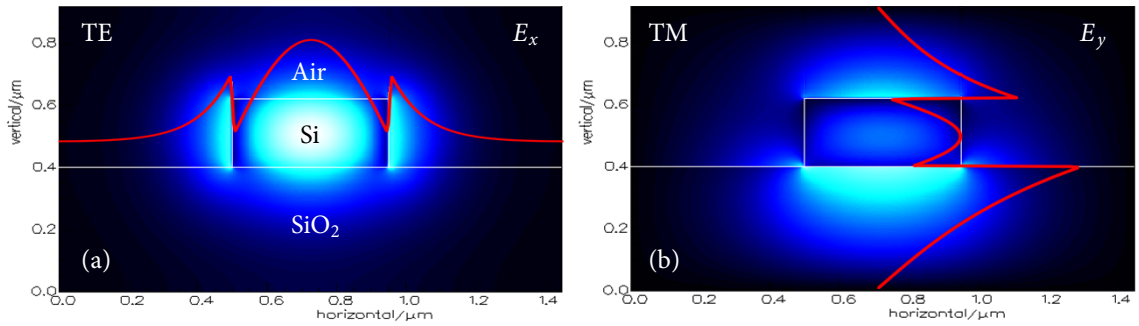

Figure 2.2: Modes in a 450 nm by 220 nm SOI waveguide simulated using FIMMWAVE. A single slice of the mode profile in the middle of the waveguide is shown inset in the figures. (a) TE mode with E_x plotted. (b) TM mode with E_y plotted.

Because Maxwell's equations state a boundary condition where the electric field parallel to the interface of two media must be continuous, there must be an electric field in the second medium or the cladding of the waveguide. The field however should not transfer any energy since it is totally reflected. The solution from Maxwell's equations is an electric field decaying exponentially with the distance from the boundary into the cladding. This field travels along the z-axis together with the field inside the core of the waveguide and is called the evanescent field. Its attenuation is given as [24]

$$\alpha = \frac{2\pi n_2}{\lambda}\sqrt{\left(\frac{n_1}{n_2}\right)^2 \sin^2\theta_m - 1} \tag{2.4}$$

with a penetration depth of $\delta = 1/\alpha$. The phase shift that occurs on TIR in formula 2.1 can be better understood by the Goos-Hänchen effect in which a lateral shift of the internally reflected beam is observed as if reflected by some virtual boundary farther away [24]. The extra distance that the beam travels to this virtual boundary and back corresponds exactly to the phase shift that is observed and the offset of the boundary is of the same order of magnitude as δ.

In formula 2.4, the fraction of the field that travels through the cladding depends on δ and thus on the refractive indices of both the core and cladding. An increase in one of the two will result in a higher n_{eff}. In figure 2.2 the evanescent tails can be clearly seen in two SOI waveguide modes. The change in n_{eff} due to a change in the cladding or ambient refractive index increases when a larger fraction of the mode energy is contained in the evanescent field instead of the core. The fraction of energy contained in the waveguide core is the confinement factor defined as

$$\Gamma = \frac{\iint_A \varepsilon(x,y)|\vec{E}|^2 \mathrm{d}x\mathrm{d}y}{\int_{-\infty}^{\infty}\int_{-\infty}^{\infty} \varepsilon(x,y)|\vec{E}|^2 \mathrm{d}x\mathrm{d}y} \tag{2.5}$$

where A denotes the area of interest which is commonly the waveguide core cross-section.

2.2 Evanescent field sensing

Sensing using the evanescent field relies on the fact that n_{eff} of a waveguide mode changes when the ambient refractive index n_{ambient} changes. In first order, this process can be described as

$$\Delta n_{\text{eff}} = \frac{\partial n_{\text{eff}}}{\partial n_{\text{ambient}}} \Delta n_{\text{ambient}} \tag{2.6}$$

where the partial derivative is dependent on factors such as the waveguide dimensions, wavelength, and mode polarization. Commonly, its value is assumed to be equal to the confinement factor of the sensing area Γ_{sense} (the air region in figure 2.2). The structure in figure 2.2 was simulated with ambient indices close to that of water in FIMMWAVE to assess this. A thin SiO_2 layer that forms when Si is exposed to air is taken into account since most of the evanescent field power is located closest to the waveguide core.

The data in figure 2.3 can be seen to converge to a point where the n_{ambient} is equal to the refractive index of SiO_2, as the waveguides are then identical. The slopes and confinement factors calculated with FIMMWAVE are in table 2.1. As expected, the slope decreases as the oxide layer increases, because there is less power is in the sensing region. The values in the last two columns of table 2.1 are of the same order of magnitude but still differ by a significant amount.

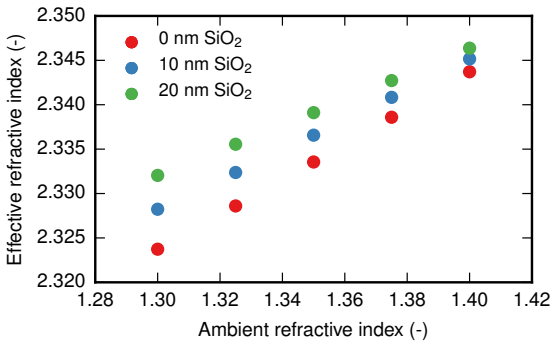

Figure 2.3: Relation between n_{eff} and n_{ambient} as simulated with FIMMWAVE for a 450 nm wide and 220 nm thick SOI waveguide and TE mode.

Table 2.1: Calculated slopes of figure 2.3 and confinement factors.

Oxide thickness (nm)	$\frac{\partial n_{\text{eff}}}{\partial n_{\text{ambient}}}$	Γ_{sense}
0	0.200	0.134
10	0.169	0.114
20	0.143	0.097

From this analysis it can be concluded that the natural oxide layer that forms on the silicon waveguide can significantly affect the sensitivity when the waveguide is used for sensing purposes. This could be a cause for variation in sensitivity between different sensors. Also of interest is that the sensitivity is apparently not equal to the fraction of power present in the sensing region Γ_{sense}, as is commonly assumed in literature.

2.3 Coupling to integrated waveguides

Coupling light from external sources into PICs and back out again can be done in different ways, three of which are shown in figure 2.4. The simplest is edge coupling, where the core of the fiber will be aligned with a waveguide on the chip that extends to the edge. As a typical 1550 nm single-mode fiber core has a diameter in the order of 8 µm, and the waveguide dimensions are in the hundreds of nanometers, the mode overlap is small and only low coupling efficiencies can be achieved.

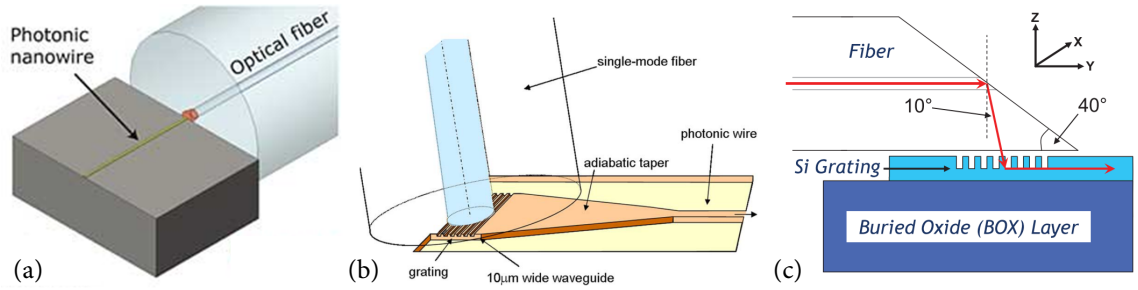

Figure 2.4: Three different methods of coupling light from fibers to into waveguides. (a) Edge coupling [25]. (b) Grating coupling [26]. (c) Grating coupling usign angle-polished fibers [27].

A problem arises when trying to couple a mode from outside with an angle into the waveguide. In order to do this the modes must be phase-matched with each other, meaning that the component of the propagation constant in the direction of the waveguide β_i must match β_m of a mode supported by the waveguide. This turns out not to be possible because of the refractive index above the waveguide core (1.0 for air) being lower than that below it (1.44 for SiO_2 in the case of SOI). A solution is to apply a grating pattern on top of the waveguide. The grating can be designed such that one of its diffracted modes will match up with a mode supported by the waveguide. Multiplying the general diffraction grating equation with the vacuum propagation constant k_0 results in [28]

$$\beta_d = \beta_i + \frac{2\pi n}{\Lambda} \tag{2.7}$$

where

β_d	diffracted mode propagation constant	(rad/m)
β_i	propagation constant component in direction of the waveguide	(rad/m)
n	diffracted mode order with $n = 0, \pm1, \pm2, \ldots$	(-)
Λ	grating period	(m).

As in formula 2.7, β_i which was initially too low can now be increased by taking the $n = 1$ diffracted mode and choosing Λ and the coupling angle appropriately to make β_d equal to a waveguide mode β_m. Typical grating periods for SOI couplers are 300 nm for 1550 nm light. As the diffracted mode angles depend on the wavelength, the grating coupler efficiency will worsen for wavelengths outside the design range. In fact, it will act like a bandpass filter around the design wavelength with 3 dB bandwidths on the order of 50 nm.

Grating couplers are very useful in the development of PICs where the space occupied above the chip by fibers is not an issue. An example is the photonic analogue of wafer-scale testing where instead of with probe needles the PICs can be tested with fibers for their performance or defects by an automated machine before the wafer is diced, something that is not possible with edge coupling. When packaging PICs in commercial products the space requirements are often harsher. For this purpose angle-polished fibers as in figure 2.4c were developed which allow the fibers to be positioned parallel to the chip surface. A polishing angle of 40° will cause light to be totally internally reflected downwards at 10°, a typical angle required by TE grating couplers.

2.4 Coupling between waveguides

The evanescent field can transfer energy when it propagates along a medium with a different refractive index. This means that when two waveguides are separated by a small distance as in figure 2.5a, energy can couple from one waveguide into the other and eventually back again. Because of this there exists no mode that can propagate indefinitely within only one of the waveguides, so this is not an eigenmode of the system. The two fundamental eigenmodes of this pair of waveguides are an anti-symmetric supermode ψ_1 and a symmetric supermode ψ_2 as seen in figure 2.5b.

Adding both supermodes or subtracting them results in a mode in either the left or right waveguide as in figure 2.5c. Because the two eigenmodes ψ_1 and ψ_2 have slightly different propagation constants they will have a beating frequency. It is this frequency that determines the rate with which energy oscillates between the waveguides. By carefully adjusting the length of a coupling region any factor κ of power transfer between two waveguides can be achieved.

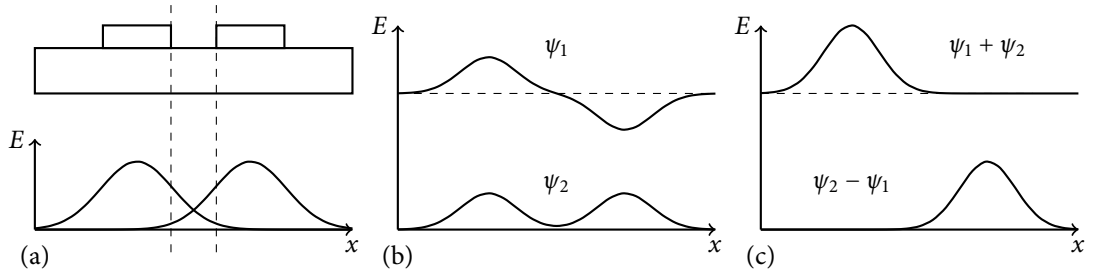

Figure 2.5: (a) Overlap of the evanescent field with another waveguide results in energy transfer. (b) The two fundamental eigenmodes of a coupled waveguide pair. (c) Sum and difference of the eigenmodes in (b).

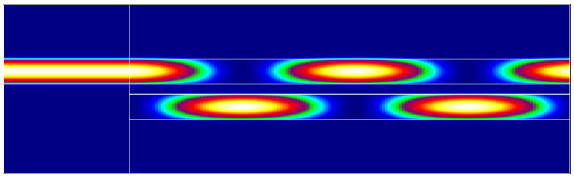

Figure 2.6: Power oscillating between two single-mode SOI waveguides by coupling simulated with FIMMWAVE, plotted is the time averaged intensity with light propagating to the right.

2.5 Multi mode interference couplers

The fact that different modes travel with different speeds through a multimode waveguide is not only a nuisance as it is for information transfer with optical fibers. In integrated photonics this is called multi mode interference (MMI). Typically single mode waveguides will be connected to a wider multi mode waveguide which then has a number of single mode output waveguides attached to it (figure 2.7). When light reaches the multimode waveguide several different modes will be excited and start travelling to the other side. Because of the difference in propagation of the modes the interference pattern will change as a function of distance. A phenomenon called self-imaging will occur where the input mode will appear in multiples of itself as in figure 2.7. [29]

By choosing the dimensions of the device appropriately the amount of output power can be optimized for the amount of output waveguides chosen. In practice electromagnetic mode solving software is used to simulate the MMI with varying dimensions. Parameters that are optimized in this way are for example the total power output, splitting ratios and phase of the outputs.

Typical dimensions of an MMI are in the order of tens of micrometers. As a consequence of the self-imaging principle, choosing a wider input waveguide increases the size of the 'lobes' inside the MMI, making it less prone to fabrication errors which can result in slightly different dimensions. This effect is clearly seen when

comparing the larger input waveguide in figure 2.7b with that of figure 2.7c. Usually a taper is used to transition from a single-mode waveguide to a wider one and into the MMI, after which the outputs are tapered back again to single-mode.

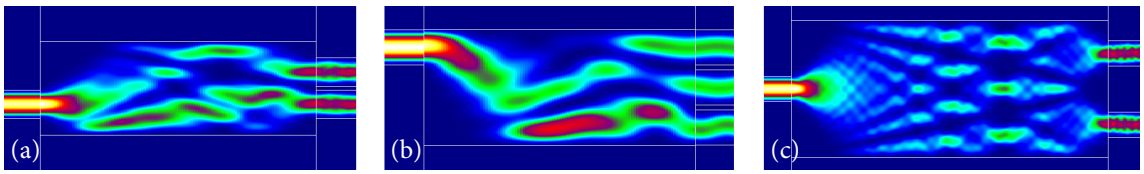

Figure 2.7: Several examples of the usage of MMI. (a) A 2×2 MMI coupler which splits the power from either input port with a 50:50 rate. (b) A similar 3×3 MMI coupler. (c) A 1×2 MMI coupler in which the possibilities for several numbers of output ports are clearly visible.

2.6 Ring resonators

Light can be coupled into a circular waveguide with circumference L using either directional couplers or MMI couplers. When this light travels around the ring multiple times it will interfere with input light, and with light that has been previously coupled into the ring. A resonating condition will occur for wavelengths that fit an integer amount of times in the circumference L because of constructive interference. These resonance wavelengths are given by

$$\lambda_{\text{res}} = \frac{L n_{\text{eff}}(\lambda_{\text{res}})}{m} \tag{2.8}$$

where $m = 1, 2, 3, \ldots$ is the mode number. The simplest configuration is that of a ring with a single waveguide next to it as in figure 2.8. This ring will function as a notch or bandstop filter to the light that passes by it when the wavelength satisfies the resonance condition in formula 2.8. After enough intensity has built up inside the ring, the mode that couples back into the straight waveguide now destructively interferes with the incoming mode, allowing almost no light to pass.

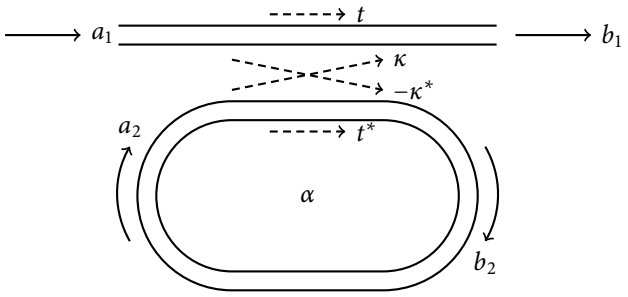

Figure 2.8: Schematic of a ring resonator with the relevant input and output amplitudes $a_{1,2}$ and $b_{1,2}$, coupling constants κ and $-\kappa^*$, transmissions t and t^*, and finally round-trip transmission α.

A theoretical model of a single ring resonator has been developed using the coupling and transmission constants between the waveguides as seen in figure 2.8 [30]. Following this model, the input and output mode amplitude and phase are related by the matrix equation

$$\begin{pmatrix} b_1 \\ b_2 \end{pmatrix} = \begin{pmatrix} t & \kappa \\ -\kappa^* & t^* \end{pmatrix} \begin{pmatrix} a_1 \\ a_2 \end{pmatrix} \tag{2.9}$$

where

$a_{1,2}$	complex input E-field	(V/m)
$b_{1,2}$	complex output E-field	(V/m)
κ	coupling constants	(−)
t	transmissions	(−).

It is defined that $|\kappa|^2 + |t|^2 = 1$ so all the light will either couple into the other waveguide or be transmitted. The transmission for light that goes around the ring is given as $a_2 = b_2 \alpha \exp(j\theta)$ with α the round-trip transmission and θ the round-trip phase gain. Combining equation 2.9 and the previously mentioned round-trip transmission gives two equations for a_1 and b_1 which can be divided by the other to result in the transmission of the ring resonator

$$T = \frac{|b_1|^2}{|a_1|^2} = \frac{\alpha^2 + t^2 - 2\alpha t \cos(\theta)}{1 + \alpha^2 t^2 - 2\alpha t \cos(\theta)} \qquad \text{with} \qquad \theta = \frac{2\pi L n_{\text{eff}}}{\lambda}. \tag{2.10}$$

Looking at the resonant condition in the first part of equation 2.10 when $\theta = 2\pi m$ it can be seen that when $\alpha = t$ the numerator tends to zero resulting in zero transmission, this is called the critical coupling condition. [30] In practice this condition is usually aimed for since it maximizes the extinction ratio (ER) which is the ratio between maximum and minimum transmission. Results for different values of α and t are shown in figure 2.9, the most preferable being equal and high values.

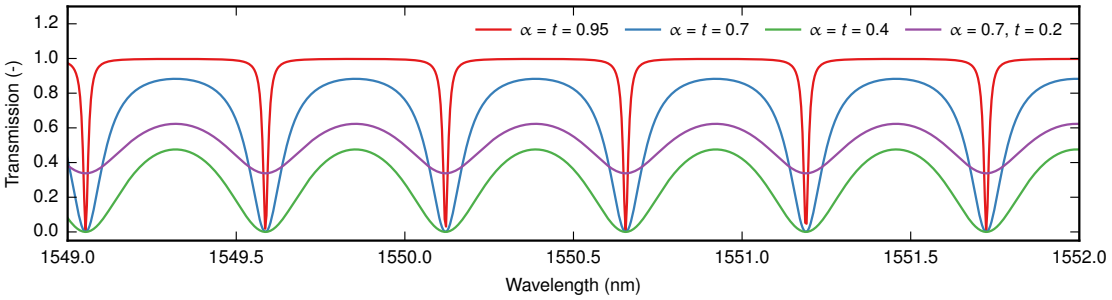

Figure 2.9: Theoretical model of ring resonator transmission according to formula 2.10. This ring has $L = 1000$ µm and $n_{\text{eff}} = 4.5$. Visible is the zero transmission for $\alpha = t$, with the maximum transmission and full width half maximum being dependent on the value of α and t.

The transmission spectrum of a ring resonator can be characterized by many of the same parameters that are also used for other optical resonators such as Fabry-Perot cavities. Important is the free spectral range (FSR) which is defined as the distance between resonances either in wavelength or frequency as

$$(\Delta\lambda)_{\text{FSR}} = \frac{\lambda^2}{n_g L} \qquad \text{and} \qquad (\Delta f)_{\text{FSR}} = \frac{c}{n_g L} \tag{2.11}$$

where c is the speed of light in a vacuum. Another important parameter is the quality factor Q which is a measure for the spectral width of the resonances.

Taking dispersion into account, the resonant wavelength shift for a change in n_{eff} can be written as

$$\Delta\lambda_{\text{res}} = \frac{\lambda_{\text{res}}}{n_g(\lambda_{\text{res}})} \Delta n_{\text{eff}} \tag{2.12}$$

where Δn_{eff} is given by formula 2.6. One particular method of interrogating a ring resonator is to measure its transmission spectrum within a fixed wavelength range with a tunable laser source, and to identify the location of the resonance wavelength(s) in this spectrum. By repeating this procedure at regular intervals, the resonance shift over time can be obtained. After a calibration with the substance of interest, this wavelength shift can be related to a change in concentration, and high-precision sensing can be performed.

2.7 Normal and three-port Mach-Zehnder interferometer

Using an MZI for sensing simplifies the read-out compared to ring resonators due to the fact that the probe wavelength is kept constant, avoiding the need for an expensive tunable laser. An MZI for usage in biosensing is usually implemented with equal arm lengths, where one of the arms is covered by a protective layer. In such a configuration, the influence of temperature fluctuations is reduced since both arms experience the same length change due to temperature. In another configuration the arms have a length difference L and an increase in n_{eff} will induce a larger phase difference $\Delta\phi$ in the longer arm. For both configurations the phase difference can be expressed as

$$\Delta\phi = \frac{2\pi L \Delta n_{\text{eff}}}{\lambda}. \tag{2.13}$$

where L stands for either the sensing window length or arm length difference for equal and unequal arms lengths, respectively. As both the interferometer arms are combined again, interference will occur provided that the light from both arms has a common polarization component. For two coherent beams with the same polarization, the resulting irradiance will be [31]

$$I = I_1 + I_2 + 2\sqrt{I_1 I_2}\cos(\Delta\phi) \tag{2.14}$$

where I_1 and I_2 are the irradiances of the two arms, respectively. From formula 2.13 it can be seen that with constant length difference and effective index, the MZI can function as a wavelength tracker. With constant ΔL and λ it will measure changes in the n_{eff}. There is however a significant shortcoming because of the fact that the output power is in the form of a $\cos(\phi)$ because the sensitivity decreases when approaching the fringe extremes, at some point even becoming zero. Additionally, once either a minimum or maximum is reached, it is unclear whether the phase is de- or increasing as the output is symmetric around this point. Both points can be solved by using an MZI with three output ports, each with a 120° phase shift between them [32]. Such output ports can be realized with a 3×3 MMI coupler, where the dimensions are adjusted to result in the required 120° phase shift between outputs. The initial splitting of the light is done with a 2×2 MMI coupler. A schematic of this three port interferometer is shown in figure 2.10a and its simulated output signals in figure 2.11.

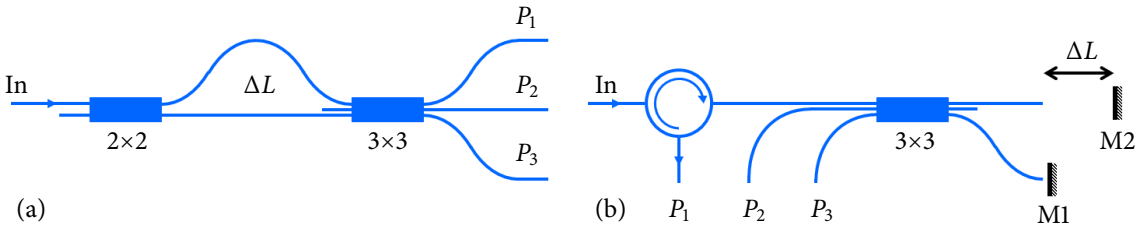

Figure 2.10: (a) Schematic of a normal three port MZI with the different parts indicated. (b) Schematic of a three port MZI in the mirror configuration.

The three port interferometer that is designed for displacement sensing (chapter 5) is in a mirrored configuration as seen in figure 2.10b. Here the input light is passed through an optical circulator and split by a 3×3 MMI of which one output channel, in this case the middle, is not used. Both outputs are reflected back into the 3×3 MMI where three interferometer outputs result in the same way as for the normal configuration. As the top channel comes back through the input waveguide, the circulator is used to extract it. Mirror M1 is fixed in position which makes this arm of constant length. Mirror M2 however can be moved back and forth and creates an effective arm length difference of $2\Delta L$.

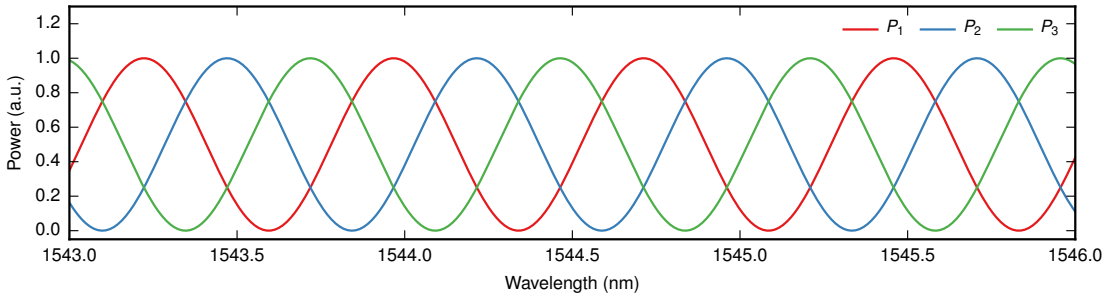

Figure 2.11: Theoretical model of the normalized output signals of a three-port MZI as a function of input wavelength with $\Delta L = 800\,\mu m$ and $n_g = 4.0$.

In order to calculate the phase from this three-port MZI, the three output signals are modeled by

$$P_n = \frac{A}{2}\left[1 + \cos\left(\phi + \frac{2\pi}{3}(n-1)\right)\right] \quad \text{with} \quad n = 1, 2, 3 \tag{2.15}$$

where

P_n	signal power	(W)
A	signal amplitude	(W)
ϕ	phase difference	(rad).

As derived in appendix B, by assuming that the amplitudes of the three signals are all equal and using trigonometric identities, the phase can be extracted from the signals with

$$\tan(\phi) = \sqrt{3}\frac{P_2 - P_3}{2P_1 - P_2 - P_3}. \tag{2.16}$$

In [33] a formula for the phase has been derived which takes into account potential offsets from the 120° phase shift between the signals. A simplified version assuming the signals are already normalized is:

$$\tan(\phi) = \frac{(\mu_2 - \mu_3)P_1 + (\mu_3 - \mu_1)P_2 + (\mu_1 - \mu_2)P_3}{(\gamma_2 - \gamma_3)P_1 + (\gamma_3 - \gamma_1)P_2 + (\gamma_1 - \gamma_2)P_3} \tag{2.17}$$

where $\mu_n = \cos\theta_n$, $\gamma_n = \sin\theta_n$, and θ_n is the phase of interferometer signal n relative to ϕ which is the phase of signal P_1. Several other blind calibration algorithms have been developed for the purpose of correcting for offsets in the signal amplitudes and phases [17, 33, 34].

The inverse tangent of a linearly increasing phase will result in a sawtooth waveform with values in the range $[-\pi/2, \pi/2]$. By using a phase unwrapping algorithm this sawtooth can be transformed into a continuously increasing or decreasing phase.

In the case of refractive index sensing, typically a calibration measurement would be made to link the calculated phase to certain concentrations of the substance of interest. As for displacement sensing, the distance that the mirror moves can be directly related to the phase via

$$d = \frac{\phi - \phi_0}{2\pi} \cdot \frac{\lambda}{2} \tag{2.18}$$

where

d	position relative to that at $t = 0$	(m)
ϕ	current phase	(rad)
ϕ_0	phase at $t = 0$	(rad).

It is clear that when the mirror M2 moves by half a wavelength, a full fringe passes in the interferometer since the light travels the distance twice.

3 Experimental details

In this chapter the simulation software, devices, measurement setups and procedures are discussed.

3.1 Mode solving and simulation software

In order to explain the observed effects of different cladding materials and waveguide dimensions on n_{eff}, n_g and the confinement factor Γ the electromagnetic mode solving software FIMMWAVE by Photon Design was used. It allows for mode-solving in various photonic structures such as strip waveguides, plasmonic devices and optical and photonic crystal fibers. The complementary FIMMPROP software can use the previously solved 2d structures to create 3d waveguides and simulate light propagation in them.

Solving Maxwell's equations exactly quickly results in long simulation times, which is why a multitude of algorithms exist that assume certain approximations to reduce computation time. FIMMWAVE offers several of these algorithms like film mode matching (FMM), finite difference method (FDM) and effective index solvers. Often one of these is the most suitable for a waveguide geometry depending on factors such as layer thickness and curved features. An often used approximation when a mode is primarily TE or TM is to calculate only the electric and magnetic fields corresponding to this polarization direction, this is called a semi-vectorial solver and can greatly reduce computation time in more complicated structures.

For the work in this project the FMM solver has been primarily used which is appropriate for the rectangular SOI waveguides.

3.2 Used instruments

As the light intensity levels in integrated photonics typically vary between tens of milliwatts to nanowatts a logarithmic scale called the dBm is often used. With a reference power of $P_0 = 1\,\text{mW}$, a value in dBm is defined as $10\log_{10}(P/P_0)$ so that a microwatt is -30 dBm and a nanowatt is -60 dBm.

For quick measurements a broad C-band (1525 to 1570 nm) amplified spontaneous emission (ASE) light source was used in combination with an optical spectrum analyzer (OSA). A C-band ASE light source works by exciting an erbium-doped fiber with a pump laser until amplification occurs. As this light travels through the doped fiber it gets amplified even more, and is efficiently coupled into an output fiber.

The Yokogawa AQ6370B OSA is a standard piece of equipment in the field of integrated photonics. It has a wavelength range of 600 to 1700 nm, can detect in an intensity range of 20 to -90 dBm and has a smallest wavelength resolution of 20 pm. It operates by rotating an internal grating on which the input light is incident and passing the diffracted light through a monochromating slit, which determines the wavelength resolution.

For more precise measurements a combination of the Agilent 81960A tunable laser source and Agilent N7744A optical power meter was used. This tunable laser has a high wavelength accuracy of 1 pm, improving the detection of the centers of the ring resonances and thus wavelength shifts. A mainframe triggers the detector to read out a power after each wavelength shift of the laser, thereby sweeping an entire range.

Measurements with the broad c-band light source are done using single mode 1550 nm fibers as the light from this source is unpolarized. Light from the tunable laser however is reasonably linearly polarized. Be-

cause the grating couplers are optimized for TE polarized light, a polarization controller is used to rotate the polarization so it is mostly TE when incident on the coupler to optimize the signal.

For pumping fluids past the chip surface, a programmable Aladdin Syringe Pump is used.

3.3 Refractive index sensing

3.3.1 Photonic chip and flowcell

The first chip that was used is called 'Design B', seen in figure 3.1, and its original purpose was to test the responses of ring resonators with various shapes, sizes and coupling methods. The rings are coupled to the input and output waveguides with MMI couplers. Also included on the chip are five three-port interferometers in a normal configuration and five in a mirror configuration as described in the theory chapter. Finally a three-port interferometer with a long ΔL of 9 mm is included. Both the normal and mirror configurations consist of a nominal 3×3 MMI of 125×7.2 µm^2 and -0.2, -0.1, +0.1 and +0.2 µm variations on the MMI width. The grating couplers are located on the left and right sides with a spacing of 25 µm between them, making read-out of two couplers close to each other on the same side impossible with fibers.

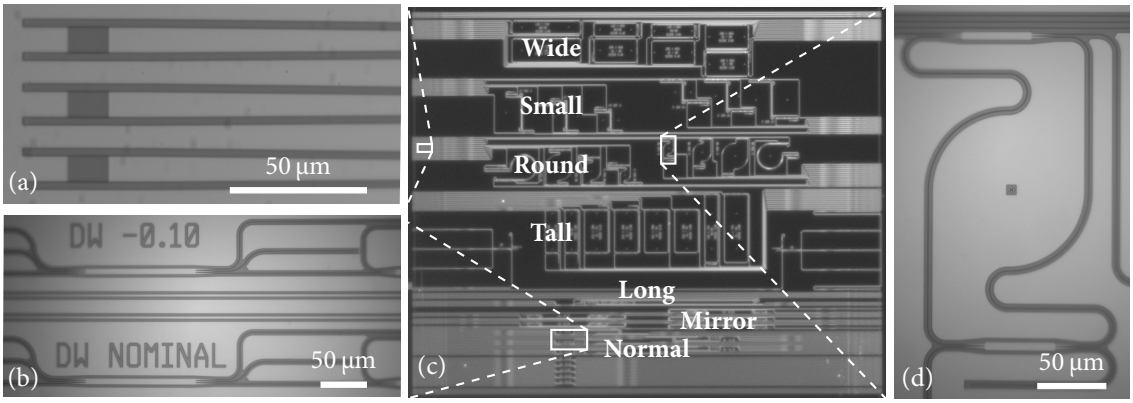

Figure 3.1: Microscope images of the Design B chip. (a) Three grating couplers, the darker areas are etched away silicon, leaving the waveguide in the middle. (b) Two 3×3 MMI couplers that are part of two three port interferometers. (c) Full view of the 6×5 mm^2 Design B chip with four rows of ring resonators on the top half indicated by their shape. At the bottom are three types of interferometers also denoted by their configurations. (d) Ring resonator with at the bottom an MMI coupler as a single add/drop port and at the top another MMI coupler with both an input and output channel so that transmission can be measured.

In order to flow fluids past the surface of the chip a small flowcell (figure 3.2) has been designed. It is machined from a piece of polymethylmethacrylate (PMMA) and designed so that it allows for laminar fluid flow past the surface for flow rates up to 85 µL min^{-1}. The flowcell can be attached to the chip surface with UV adhesive after which two short pieces of rigid tubing are inserted in the holes on both sides and glued in place to allow for flexible tubing to be attached.

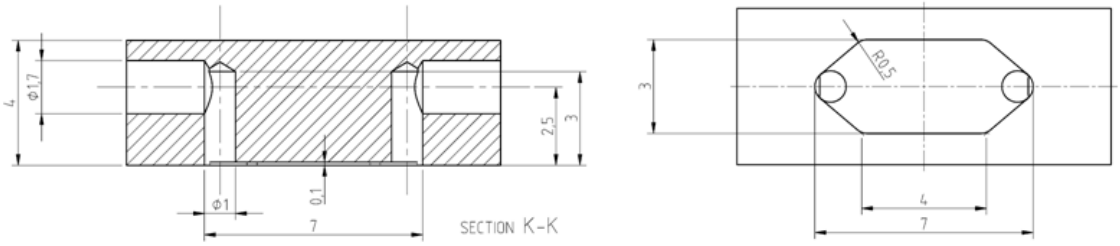

Figure 3.2: CAD model of the flowcell. (Left) Side view. (Right) Bottom view. The angled corners in the channel are to prevent fluid from getting trapped as would happen in the coners if the channel were to be rectangular.

3.3.2 Single channel readout

As the Design B chip uses grating couplers for both input and output, transmission measurements of a single channel are done with two cleaved single-mode 1550 nm fibers at an angle of 10° relative to the surface normal of the chip. The coupling efficiency is very sensitive to the position of the fiber, requiring a positional accuracy of several micrometers for proper alignment. This control is provided by two XYZ translation stages as seen in figure 3.3 that can be adjusted with micrometer accuracy.

The chip is placed on a vacuum chuck which holds it firmly in place when a pump is turned on so that changes in the alignment during measurements are prevented. The chuck is an aluminium block that is thermally isolated from the rotation and translation stage with nylon screws as in figure 3.3b. Inside the chuck is a thermistor as temperature sensor and Peltier element that are used in combination with a PID controller to provide temperature control of the chip.

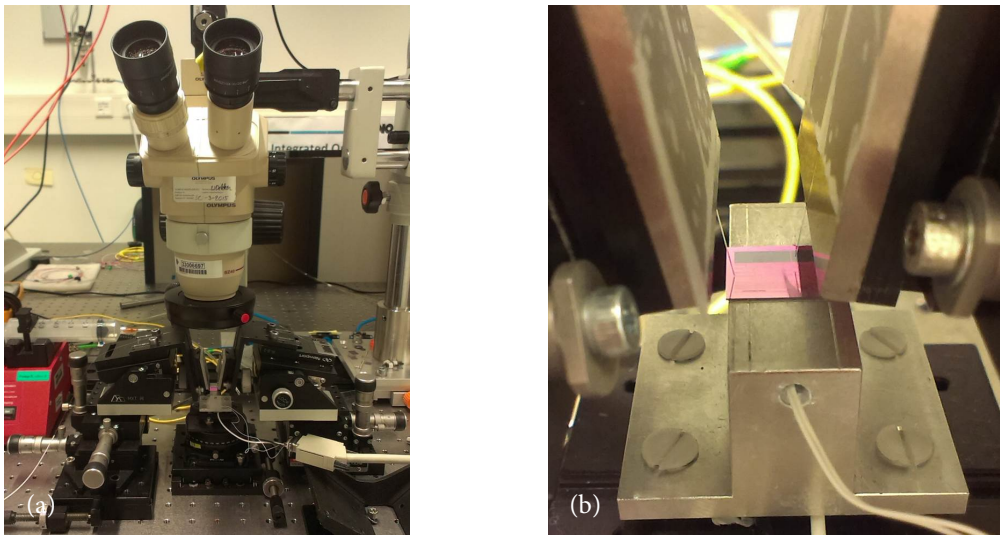

Figure 3.3: The setup used for simple transmission measurements. (a) Front view of the setup excluding light source and detector. The light comes in from either the left or right side and is read out from the other side. Fiber XYZ translation stages are left and right of the central chip stage. (b) Close-up of the vacuum chuck. Below the chip is a hole which is pumped vacuum in order to secure the chip.

In order to align a chip for measurements both fibers are first translated a centimeter away from the chuck. The chip is then placed on the vacuum chuck and secured by turning on the pump and chuck valve. The chip is rotated so that the fibers are in line with the waveguide direction. The ends of both fibers are brought closer to the chip surface whilst tracking their shadows to prevent contact as the fibers are easily damaged. A broad c-band light source and OSA or tunable laser and detector are turned on and the fibers are translated along the surface plane of the chip to find the optimal alignment position.

3.3.3 Multiple channel readout

For measurements of the interferometers it is essential that the three output signals are measured simultaneously. With the Design B chip this cannot be done with fibers because of the spacing or pitch between grating couplers of 25 µm being much smaller than the fiber cladding diameter of 127 µm. A solution is to use an infrared camera to image the light coming out of the grating couplers. With this method a large number of channels can be read out simultaneously.

A Xenics Xeva 1.7-640 IR camera with a resolution of 640×512 pixels, maximum framerate of 25 Hz and 14-bit resolution was used. In order to be able to adjust the magnification the camera was mounted on a Navitar 12x zoom lens system. The final magnification is done with a Mitutoyo 20x long working distance objective which is needed to stay clear of the flowcell attached to the chip surface as in figure 3.4b.

Because the objective is located directly above the chip, there is no room for an input fiber as in figure 3.3b.

The solution is to use an angle-polished fiber as in figure 2.4c. In figure 3.4b the angle-polished fiber is visible on the left, mounted in a fiber rotator with which the direction of the beam emitted by the fiber is adjusted.

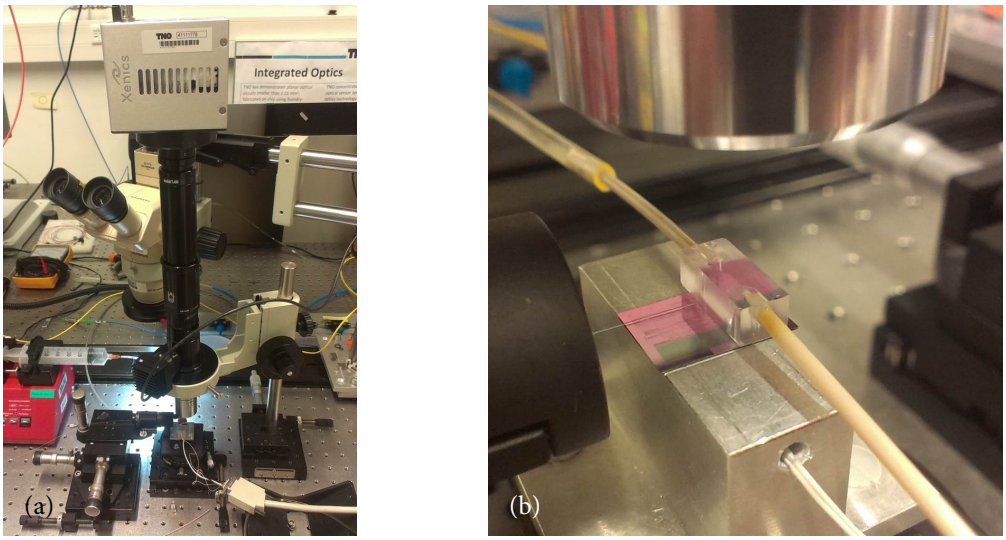

Figure 3.4: The setup used for multiple channel readout. (a) View of the full setup without light source and detector. On the left side of the chip is the angle-polished input fiber on an XYZ translation stage. On the right side the camera mount is attached to an XYZ stage. (b) Close-up of the chip with flowcell in the setup. The angle-polished input fiber can be seen positioned over the surface of the chip.

3.3.4 Fluid measurements

In order to pump fluids through the flowcell along the surface of the chip a programmable Aladdin syringe pump was used. The pump is set to withdraw the syringe so fluid containers at the other end can be changed to switch the type of fluid. Because of the flowrate of 85 µL min^{-1} it takes around 9 minutes for changes in the fluid to reach the chip.

It is important that the fluids can be switched without introducing air bubbles into the tubes. When a bubble passes over the ring resonator or interferometer the refractive index change is so high that the response shifts a multitude of FSRs. The measurement speed is not fast enough to track this and the absolute wavelength shift is lost. Switching is done by removing the tube from the container and holding it downwards so that a drop forms at the end, when it is passed into the second container no air can enter the tubing.

Solutions of 3, 6, 9 and 12% mass percentage salt corresponding to a range of 0.02 RIU were fabricated for the measurements using de-ionized water and NaCl (31434, Sigma Aldrich). The refractive indices of the solutions were calculated with an empirical formula that is valid for a wavelength range of 1530 to 1565 nm and NaCl mass percentages up to 25% [35]. All measurements were started with a de-ionized water baseline.

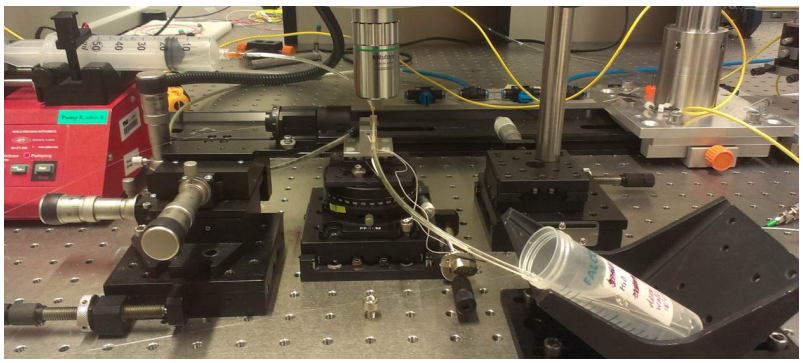

Figure 3.5: A view of the fluid routing. The syringe pump in red is on the left. Fluid containers are held on the right.

3.4 Displacement sensing

3.4.1 Photonic chip

The photonic chip that is used for displacement sensing (figure 3.6) was originally developed as a compact and low-cost fiber Bragg grating (FBG) read-out unit using 3×3 interferometers. A test circuit for displacement sensing (figure 2.10b) was included on the chip because this did not increase the costs of production. The chip is fabricated by making use of the JePPIX platform which is specialized in InP photonics.

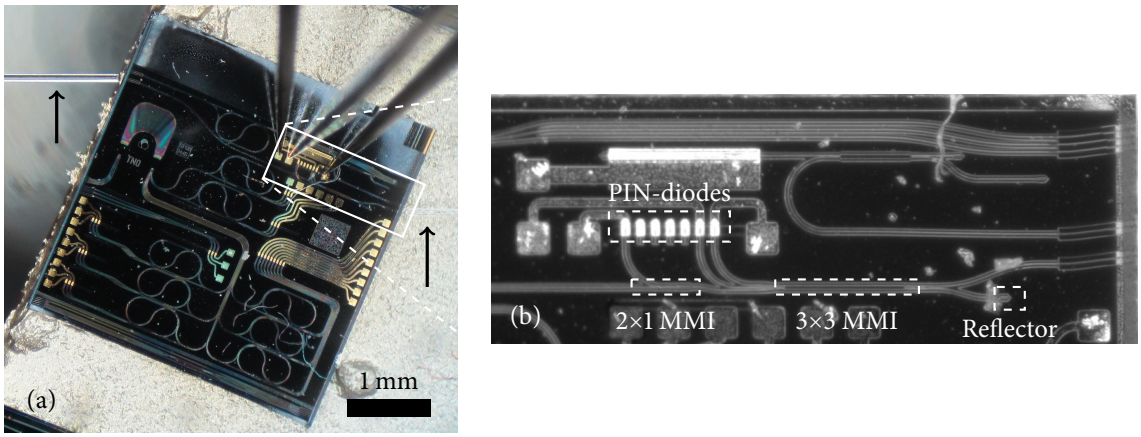

Figure 3.6: Microscope images of the displacement chip. (a) Full view of the chip with a lensed fiber on the left providing the light and one on the right going to the external mirror. The fibers are marked with black arrows for clarity. Also visible are the probe needles contacting the PIN-diode anodes. (b) Close-up of the primary part of the circuit.

The 3×3 interferometer on this chip is of the mirrored configuration as discussed in the theory chapter. Because optical circulators do not exist as integrated optical components a 2×2 MMI is used which results in a 50% power loss to the interferometer and an additional 50% loss in the signal extracted with this MMI.

Getting light into the waveguides is done by edge coupling. The coupling efficiency is increased by having the waveguides that extend off to the edge of the chip tapered from a width of 1.5 to 3.5 µm and using a lensed fiber to focus the light at a point 5 µm in front of the fiber. To avoid reflections by the waveguide facets from creating cavities, the waveguides are extended to the chip edge at an angle of 7° relative to the edge normal as seen on the far right of figure 3.6b. As a consequence of refraction the lensed fibers have to be positioned at a larger angle of 23° to the edge normal (top left of figure 3.6a).

The cathodes of the PIN photodiodes on the chip are connected to the substrate to function as a common cathode and halve the amount of bonding pads needed. By glueing the chip to a small copper bar with conducting glue this common cathode is easily connected.

3.4.2 Measurement setup

A schematic view of the setup is shown in figure 3.7. In order to direct light from one of the interferometer ports to a mirror and back into the chip several components are used. First of all the light is coupled into a fiber with a lensed end. At some point this fiber is then cleaved and positioned into the focal distance of a microscope objective to create a collimated beam. The mirror that reflects this beam back again has to be aligned so that as much of the beam power as possible is focussed back into the fiber and returned to the chip.

While this chip has been tested for usage as a displacement sensor before, it turned out that the length of the fiber between the chip and the mirror had a large influence on the noise level of the interferometer signals. This was found to be due to wavelength noise of the laser. With a fiber length of 3 m and 1.5 refractive index, the effective distance that the light travels to the mirror and back is as much as 9 m. In this case wavelength noise in the order of 10 fm will cause an effective arm length noise of $(9/1550 \cdot 10^{-9}) \cdot 10 \cdot 10^{-15} \approx 58$ nm. Accordingly, the aim of this setup is to use as short of a fiber between the chip and mirror as possible. The

lensed fiber is cleaved at a length of 11.5 cm and the distance between the fiber and mirror is 5.5 cm, resulting in an effective distance of 45.5 cm, and reducing the influence of wavelength noise by a factor of $9/0.455 \approx 20$. A consequence of such a short fiber is that the alignment of the fibers to the chip and the fiber to the objective and mirror cannot be carried out separately as was done in the previous test.

The setup (figures 3.8 and 3.9) was built in such a way that every individual component except for the chip can be translated in every direction with micrometer accuracy using Thorlabs NanoMax stages. Mirror M2 is attached to a tiltable mirror holder and can be translated in a range of 20 µm for 0 to 75 V using the piezoelectric actuators of the NanoMax stage. The stage is driven by a Thorlabs piezo controller that converts signals from a range of 0–10 V to 0–75 V. For the input a function generator is used of which the output is also sampled with a National Instruments ADC at 10 kHz as reference.

The bonding pads of the three PIN photodiodes are contacted using tungsten probe needles (figure 3.9). As typical currents are on the order of a microampere, a transimpedance amplifier (TIA) consisting of TL072 general purpose op-amps is used to convert the currents to easily measurable voltages. A resistor of 100 kΩ and capacitor of 10 pF result in a gain of 10^6 V/A and bandwidth of 10 MHz. All channels are passed through an analog low-pass filter cut off at 5 kHz to improve the signal-to-noise ratio and finally sampled with the ADC at 10 kHz.

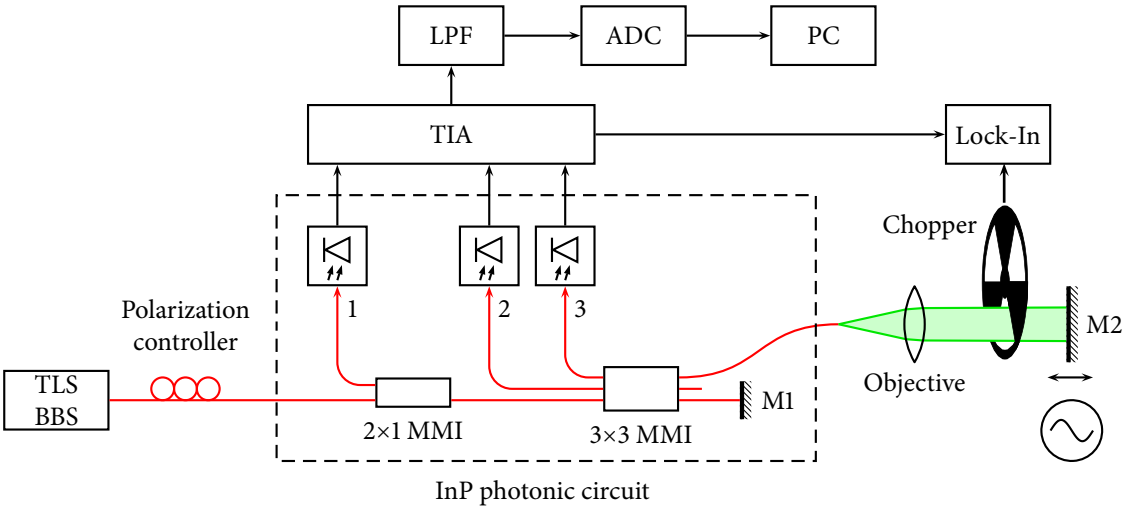

Figure 3.7: Schematic of the measurement setup for the displacement sensor. For alignment a broad C-band source (BBS) is used and for displacement measurements a tunable laser source (TLS). After alignment the chopper is removed from the setup.

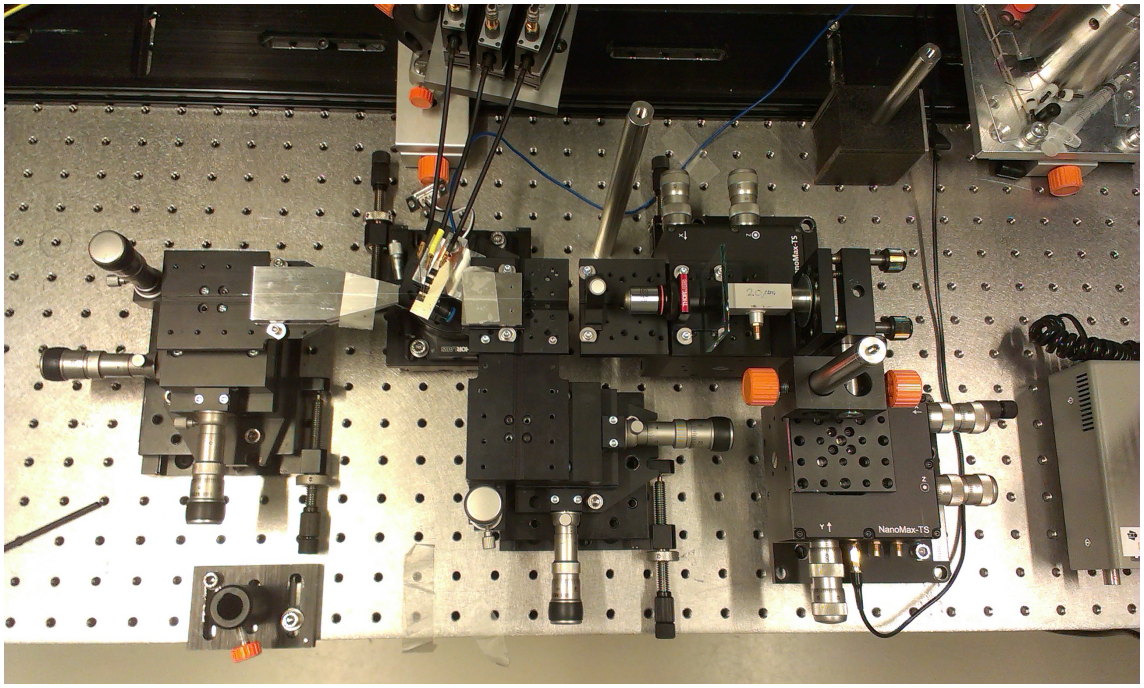

Figure 3.8: Top-down view of the setup.

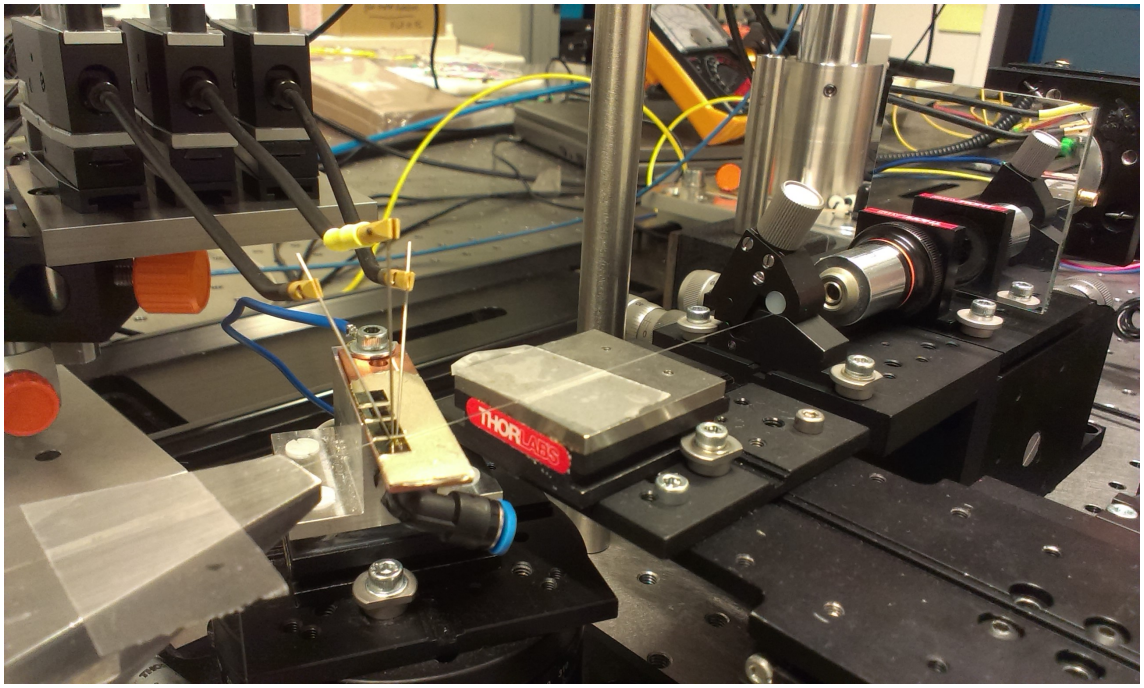

Figure 3.9: Closer view of the optical path.

3.4.3 Optical alignment

First of all a lensed fiber connected to the broad C-band source is aligned to the input waveguide. Due to mirror M1 in figure 3.7 there will always be some reflection back into all of the photodiodes, providing a signal. The position of the lensed end is adjusted until a photodiode signal is observed which is then further optimized.

After the input fiber is in place, the fiber of 10 cm with a lensed end on the side of the chip and cleaved end on the other is placed into the setup. Positioning of the lensed end to the output waveguide of the chip is done by sight until a spot from the cleaved end of the fiber is observed with an IR camera. The intensity of the spot is optimized by adjusting the position of the lensed end (right side of figure 3.6a). The cleaved end of the fiber is then fixed in position with a fiber clamp (figure 3.9) so the lensed end can be readjusted without disturbing the alignment of the objective and mirror (figure 3.10).

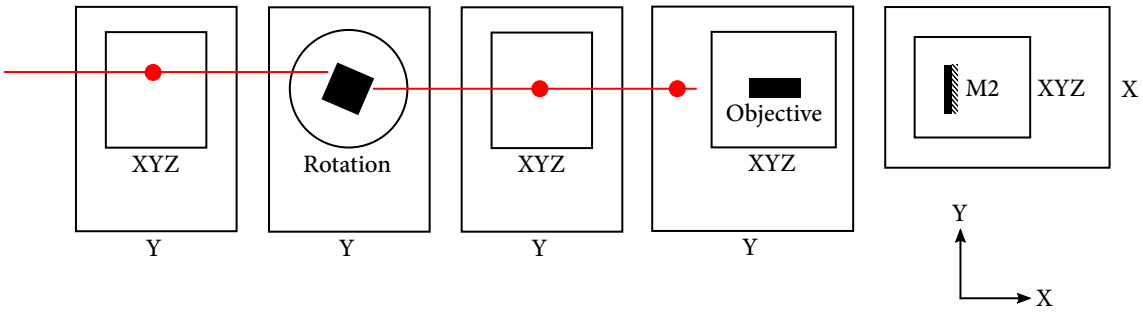

Figure 3.10: Schematic view of the stages in figure 3.8. X, Y, XYZ, or Rotation denotes the directions in which the stages can be moved. Single-letter stages are for coarse longer range movement. The red dots denote places where the fiber is fixed to the stage. Fixing the second fiber in two places allows both sides to be optimized without disturbing alignment of the other.

Aligning the objective and mirror was first separately tested to see what coupling efficiencies are attainable. A fiber circulator and power meter were used to assess the power coming back from the fiber. Initial alignment was done using red light until light is seen to be scattered from the fiber cladding. After this the C-band source was used and the alignment is optimized with the power coming back from the fiber. Losses of only −3 dB were possible this way. Repeating the procedure without knowledge of the reflected power and purely by sight using only the C-band source and IR camera a loss of −20 dB was reached.

As the coupling loss from the chip into a lensed fiber is on the order of −6 dB, alignment using only the IR camera results in a photodiode signal that is $-6 - 20 - 6 = -32$ dB lower than the signal due to mirror M1. Because this is a tiny signal compared to the background, and completely obscured by noise, a lock-in amplifier is used for further alignment. A chopper is placed between the objective and mirror to modulate the photodiode signal due to mirror M2. The chopping frequency is carefully chosen to avoid any 50 Hz harmonics. Again the broad C-band source is used because using a single wavelength as would be done for displacement measurements will result in fringes, and due to adjustment these fringes will change making optimization of the signal impossible. By adjusting the objective position and mirror tilt, the lock-in output is optimized and the previously measured loss of −3 dB is attainable, resulting in a power difference of $-6-3-6 = -15$ dB between the light arriving in the interferometer due to mirror M1 and M2.

4 Refractive index sensing results

4.1 Device selection

In order to make a judgement about the use of a three port interferometer as biosensor, a comparison of the sensitivity was made with other ring resonators on the same chip. First, the ring resonator and interferometer transmissions have been measured in order to select the best devices with which to continue the comparison. These measurements were done with a broad C-band light source and OSA as described in the methodology. The selection criteria are not very hard, a ring resonator response needs to show a relatively clean signal with a decent extinction ratio of 10 dB or higher. Figure 4.1 shows two ring responses that fit these criteria. The FSR is automatically determined by finding the peak in the results of a fast Fourier transform (FFT). For each of the four shapes of ring resonators two were selected that fit the criteria and can be used for comparison with the interferometers.

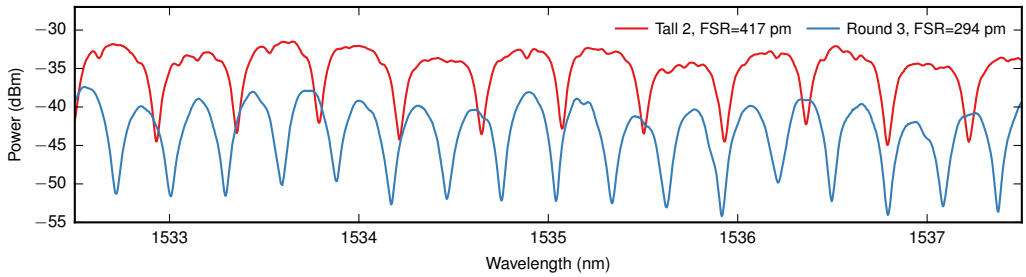

Figure 4.1: OSA transmission measurement results of two different ring resonators on the chip. They have a different FSR and absolute signal power but otherwise equal extinction ratio and FWHM of the resonance peaks.

The selection criteria for the three-port MZIs is which device produces outputs that resemble the cleanest sine function. As can be seen in figure 4.2, there are low and high frequency modulations of the interferometer signals. These results are representative for all the normal three-port MZIs on the chip. The MZIs in a mirror configuration show significant deformations in their response and are not further measured.

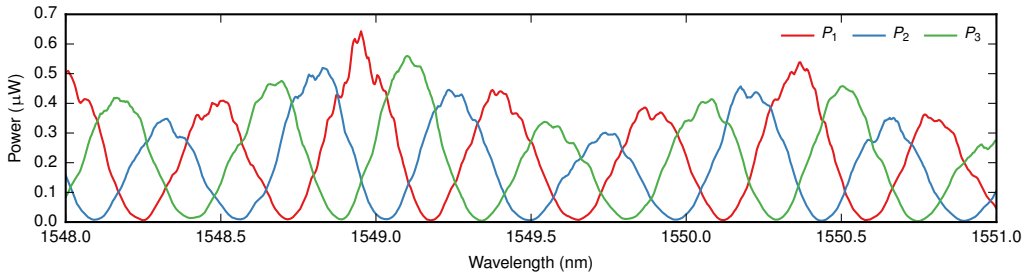

Figure 4.2: OSA transmission measurement results of the normal +0.1 µm three port interferometer. Clear low and high frequency modulations of the interferometer signals can be seen.

Following this, higher resolution transmission measurements were made with the tunable laser and detector which have a wavelength resolution of 1 pm compared to the 20 pm of the OSA. This also allows for more

accurate analysis of the higher frequency modulations. The measurements were done over a large wavelength range of 1520 to 1570 nm, providing good resolution in the FFT. For the FFT the wavelengths are converted to frequency via $f = c/\lambda$ as the FSR is then constant (formula 2.11) which results in narrower FFT peaks.

A ring response measured with the tunable laser is shown in figure 4.3. The strongest peak in the FFT is located at a periodicity of $1.83 \cdot 10^{-11}$ Hz^{-1}, the inverse of which is the FSR in frequency of 54.6 GHz. Using formula 2.11 and assuming a group index of 4.5 the ring length is calculated to be $L = c/n_g\Delta f = 3.00 \cdot 10^8/4.5 \cdot 54.6 \cdot 10^9 \approx 1220$ µm. The two peaks on the right are higher harmonics of the fundamental ring resonator FSR. More interesting is the lowest frequency peak at $5.82 \cdot 10^{-12}$ Hz^{-1}. Calculating the corresponding length not for a ring resonator but for a Fabry-Perot cavity where the relation is $L = c/2n_g\Delta f$ because of the light travelling twice through the cavity and using the Si substrate n_g of 3.63 results in a length of 240 µm. This corresponds well to the actual Si substrate thickness of 250 µm indicating that the low frequency modulations of the ring response are probably caused by the substrate acting as a Fabry-Perot cavity. This belief is further strengthened by the fact that the backside of the substrate has been polished for the purpose of reading out the grating couplers from the backside of the chip. Polishing results in a highly reflective surface, making the substrate likely to act as a cavity. A newer generation chip of which the backside was not polished does not show these low frequency modulations.

The higher frequency modulations result in a peak in the FFT at $2.26 \cdot 10^{-10}$ Hz^{-1} not shown in the FFT in figure 4.3, the inverse of this is an FSR of 4.42 GHz. Assuming a Fabry-Perot cavity and a group index of 4.5 this peak corresponds to a cavity length of $L = c/2n_g\Delta f = 3.00 \cdot 10^8/4.5 \cdot 4.42 \cdot 10^9 \approx 7530$ µm. This again can be clearly shown to correspond to a structure on the chip, namely the input and output grating couplers of this particular ring resonator which are located 7533 µm apart. It can thus be concluded that the grating couplers have some small reflections for incoming light, resulting in another cavity. For newer generation chips the coupler design was changed to a focussed grating coupler and the high frequency modulations were suppressed, indicating much lower reflections.

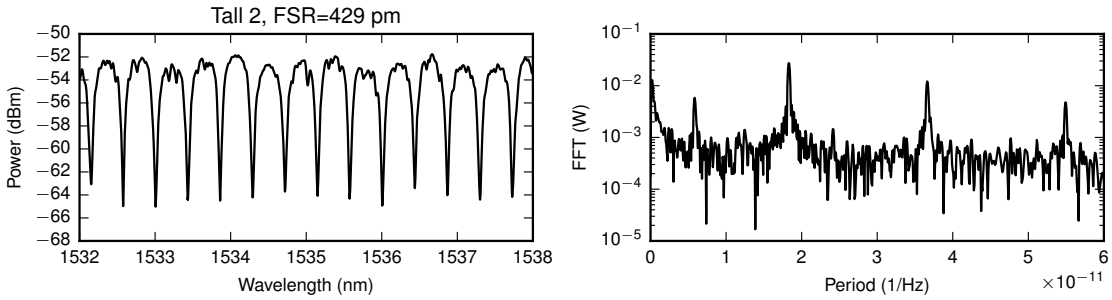

Figure 4.3: Tunable laser transmission measurement results of the second tall ring resonator. All the significant peaks in the FFT can be attributed to physical features of and on the chip.

Similar measurements and analysis was done for the three port interferometers, a typical result is shown in figure 4.4. The strongest peak in the FFT corresponds to the interferometer FSR of 462 pm. Again the lowest frequency peak due to the substrate acting as a cavity is present. The two lower peaks around the interferometer FSR are frequency products of the lowest frequency peak and that of the interferometer.

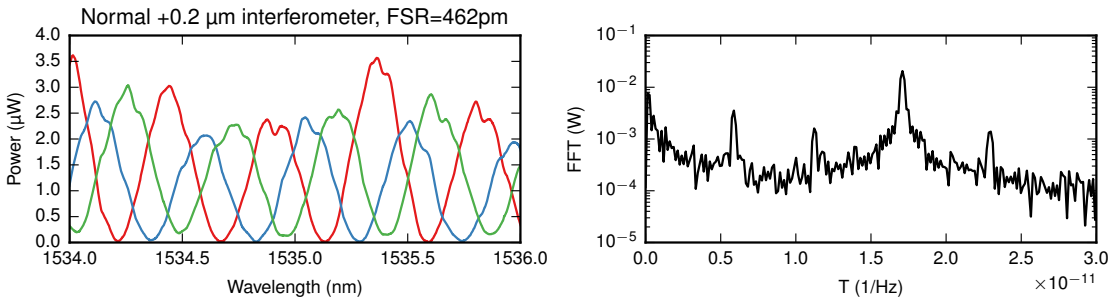

Figure 4.4: Tunable laser transmission measurement results of the normal +0.2 µm three port interferometer.

From these measurements it is concluded that the normal and long interferometers will be used to compare sensitivity as a biosensor. The long configuration is especially promising since a change in refractive index will result in a tenfold increase of fringes passing by, also potentially increasing the sensor sensitivity by a factor of ten. Because the low and high frequency modulations can be attributed to Fabry-Perot cavities formed by various reflections on the chip, they are not caused by defects in the 2×2 and 3×3 MMI couplers used in the three port interferometer. This means that for measurements with a constant wavelength, which will be done for biosensor tests of the interferometer, the modulations should stay constant. As a result the signals will not contain the modulations and result in better calculation of the phase from the three signals.

4.2 Salt solution measurements

4.2.1 Ring resonators

Two measurements of NaCl solutions with the second tall ring and sixth wide ring are shown in figure 4.5. Linear fits of the wavelength shifts result in sensitivities of 40.48 nm/RIU for the tall ring and 113.07 nm/RIU for the wide ring. A sensitivity of 113.07 nm/RIU is of a similar order of magnitude albeit lower than those obtained in other ring resonator sensors like 163 nm/RIU [19]. The difference in sensitivity between the tall and wide ring is attributed to a large part of the tall ring consisting of 3 µm wide waveguides instead of the standard 450 nm. The confinement factor of the wider waveguide is larger, meaning that the mode power is better contained inside the core and there is thus less interaction of the evanescent field with the fluid.

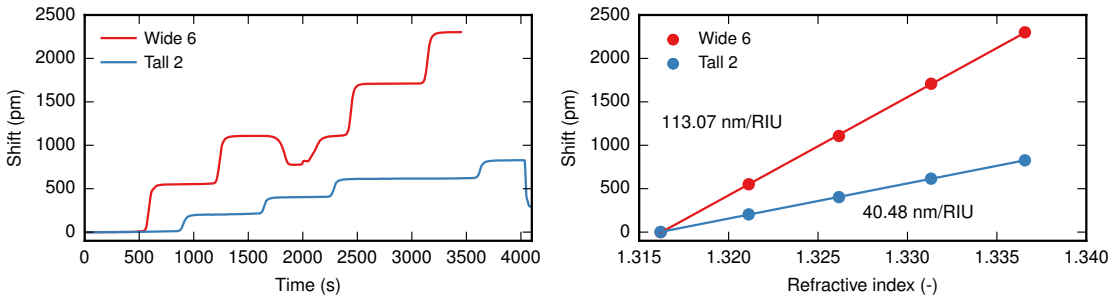

Figure 4.5: (a) Two separate measurements of two ring resonator responses to a baseline of demiwater and successive 3, 6, 9 and 12 percent salt solutions. The dip in the middle of the tall ring response is due to a short period of accidental reverse pumping. (b) Shifts for each salt solution are obtained by averaging the flat parts in (a). For both measurements a good linear fit of the data resulting in the sensitivity is obtained.

Data processing is done by the existing FRESCO software. Wavelength sweeps from 1530 nm to 1540 nm are carried out roughly every second. The software first passes the data through a low-pass filter to remove a DC offset and trend. After this it is high-pass filtered to reduce the noise levels. The wavelength sweeps are finally interpolated using a sinc function and cross-correlated with the previous sweep to determine the shift of the resonance dips. Sinc interpolation increases the 1 pm wavelength resolution of the laser and allows the result of the cross-correlation to have 0.1 pm resolution.

To determine the limit of detection (LOD) the noise level in a detrended flat part of the wavelength shift signal is calculated as $3\sigma \approx 0.279$ pm. From the noise level and the sensitivity an LOD of $0.279/113.07 \cdot 10^{3} \approx 2.47 \cdot 10^{-6}$ RIU is found.

4.2.2 Interferometers

A concentration measurement using the −0.1 µm variation 3×3 interferometer which has a path length difference of 1050 µm can be seen in figure 4.6. After the measurement is done, the recording that was taken with the camera is processed to retrieve the three signals. First, three regions of interest are defined and the maximum pixel value in each of these is found for every frame of the recording. All pixel values are then passed through the mapping function in figure 6.1b in appendix C to correct for non-linearity. After this

the three signals are divided by their respective maxima to correct for power imbalances. Finally the phase, which is the parameter of interest, is calculated from the normalized signals and unwrapped.

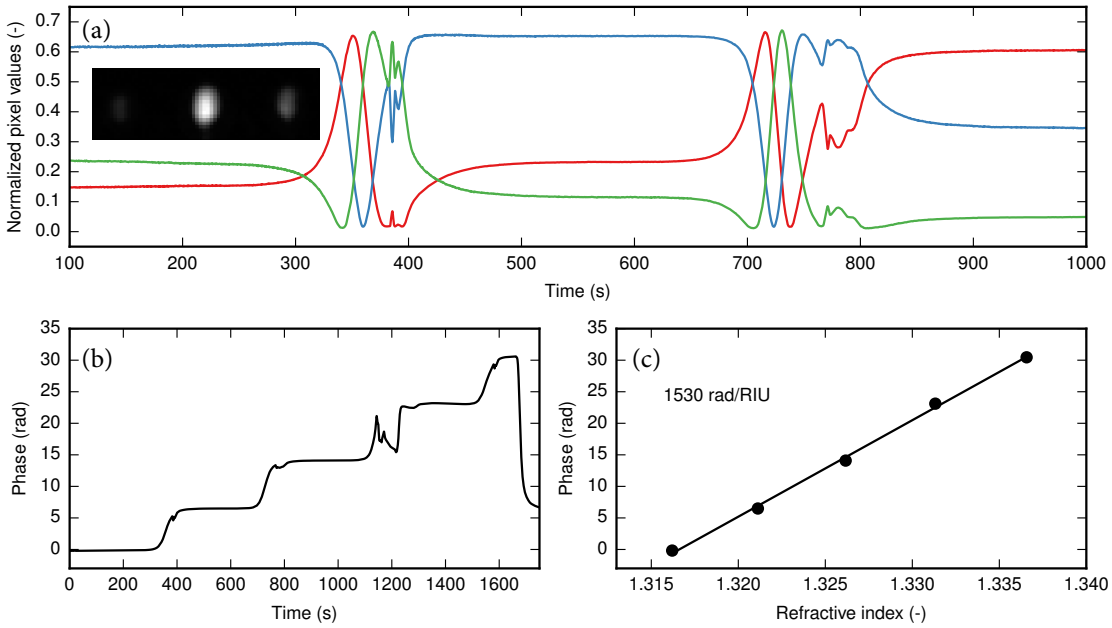

Figure 4.6: Results from a measurement of demiwater and 3, 6, 9 and 12 percent salt solutions using the normal −0.1 µm three port interferometer at a wavelength of 1540 nm. (a) The signals from the three ports are extracted by taking the maximum value from the three regions of interest for each frame. A smaller part of the full measurement is displayed in order to show two transitions more clearly. Inset is the first frame of the measurement with from left to right the red, blue and green signals. (b) Phase calculated from the three signals, the dip at around 1200 seconds is due to accidental pump reversal. (c) Phase shifts for each of the solutions averaged from (b) with a linear fit resulting in the phase sensitivity.

Since the IR camera detects photons, the resulting signals will contain shot noise due to the quantization of light. In theory shot noise is a type of white noise because it has a constant power spectral density (PSD). The noise power will thus increase linearly with the bandwidth or frequency of the detector. An FFT of one interferometer signal in figure 4.7 shows this flat background clearly. However, there are three weak peaks visible at 0.75, 1 and 2.4 Hz. Comparison with the other two signals of the interferometer bandpass-filtered around these frequencies shows that they are correlated with each other. Performing an FFT on the center of gravity of the spot in every frame of the recording results in the same frequencies. This means that they can be attributed to very light swaying motion of the microscope and infrared camera combination seen in figure 3.4a. The combination is quite heavy and is mounted in a rubber ring at the holder located at the bottom which results in the low frequency camera movement that is seen. Proper mounting of the microscope should eliminate these frequencies.

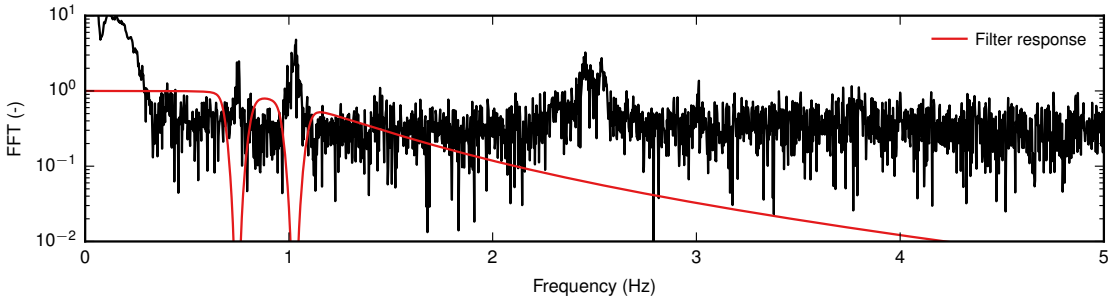

Figure 4.7: Frequency spectrum of one of the three unfiltered interferometer signals during a salt concentration measurement. In red the frequency response of the used low-pass filter and two notches around the strongest peaks caused by camera movement.

Because the interferometer signals for the used concentrations do not change faster than about 1 Hz, a lowpass

filter shown in figure 4.7 reduces most of the flat background caused by shot noise. Additional notch filters remove oscillations caused by the camera swaying. A fairly linear part of the measurement from 930 to 1020 seconds gives a noise level of $3\sigma \approx 0.0037$ rad. Knowing the sensitivity, this phase noise gives an LOD of $3.7 \cdot 10^{-3}/1530 \approx 2.4 \cdot 10^{-6}$ RIU. This LOD is nearly equal to that of the wide ring resonator on the same chip that was also measured. There is still much to be improved upon since this interferometer was not designed for usage as a biosensor.

Measurements of the longer interferometer with a path length difference of 9000 µm (figure 4.8), roughly nine times greater than the normal interferometers, result in a sensitivity of 13051 rad/RIU scaling linearly with the length. After filtering the signals with the filter response similar to that in figure 4.7 but with the low-pass cut off at 3 Hz, the phase noise is $3\sigma \approx 0.143$ giving a detection limit of $0.143/13565 \approx 1.1 \cdot 10^{-5}$ RIU. This worse detection limit is the result of the longer path difference creating a power imbalance at the point where both arms come together due to losses in the longer arm. The imbalance leads to a poor fringe resolution allowing only the top 12% of the full pixel range to be used and resulting in a signal-to-noise ratio that is much lower than that due to normal shot noise. While the sensitivity is a factor nine greater, the signal-to-noise ratio degrades the detection limit significantly. Such a problem could be solved by introducing power splitters to the short arm to balance the power and restore the fringe contrast.

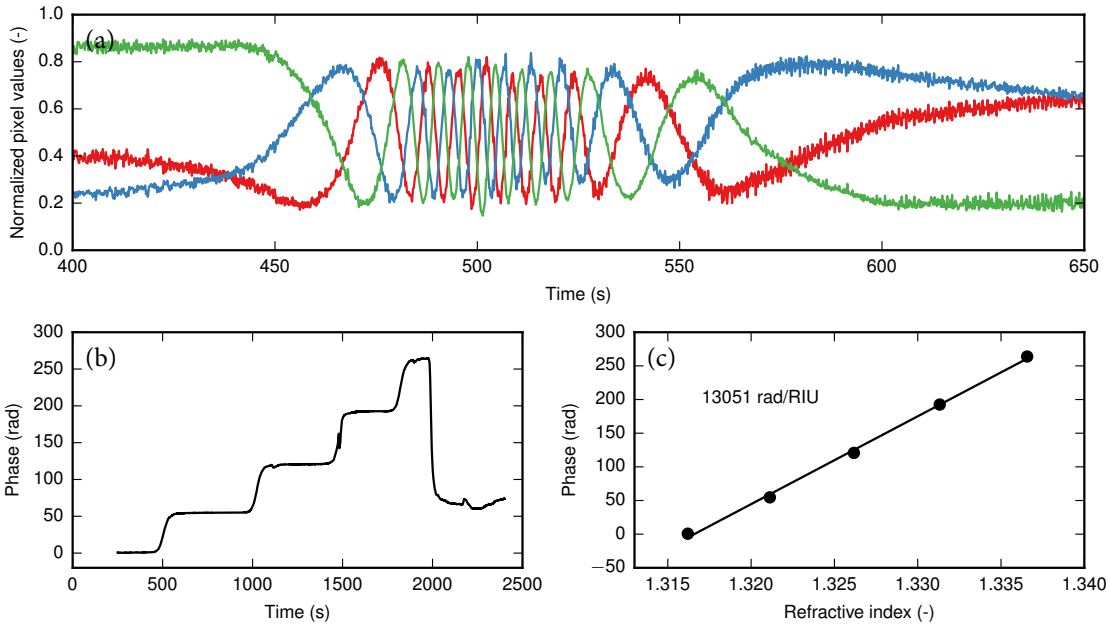

Figure 4.8: Similar measurements as in figure 4.6 but for an interferometer with a path length difference of 9000 µm, about nine times greater than the normal interferometer. In (a) the roughly ninefold increase in fringes for a single transition can be clearly seen.

4.2.3 Photodetector measurement

In a practical case the chip would not be read out using an IR camera as this is a very costly and large solution. On- or off-chip photodetectors provide more accurate results whilst being low in cost and size. To see how the precision of the measurements taken with the IR camera compares to a photodetector, a single channel of the interferometer was measured with a Thorlabs PDA10CS InGaAs detector. Slight vibrations in the fibers above the chip turned out to change the coupling efficiency to be the largest noise factor, so two angle-polished fibers were positioned for optimal coupling and then fixed to the chip surface with UV adhesive. Salt solution measurements resulting in at least a single fringe passing by were carried out to assess the typical noise levels achievable with a photodetector.

In figure 4.9 a measurement at 200 kHz of a single interferometer output for a transition from demiwater to 6% salt solution is shown. The strongest peaks in the frequency spectrum are 50 Hz power line cycles and higher harmonics. Since the fringes due to refractive index changes are of much lower frequency, the data is

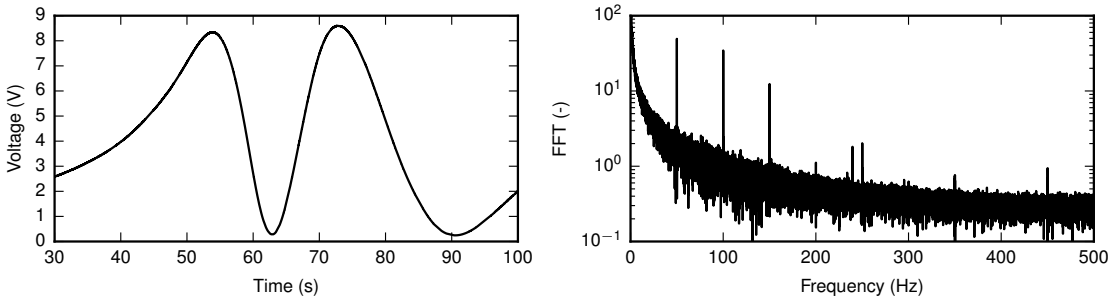

Figure 4.9: (a) A transition from demiwater to 6% salt solution. (b) FFT of the transition, showing primarily noise from the power line frequency and harmonics.

downsampled to 50 Hz by averaging every 4000 sequential values. A fifth order polynomial is fitted to one of the peaks of the transition as in figure 4.10 and subtracted from the measurement yielding a noise level of $\sigma = 773\,\mu V$. When divided by the signal amplitude of 8.6 V this results in a relative noise level of 0.0090%.

The effect of this noise in the individual signals on the calculated phase is evaluated using the error model derived in appendix B. Three ideal interferometer signals were modelled with a noise level scaling with the square root of the signals (assuming it is primarily due to shot noise) to a maximum of 0.0090%. The maximum noise in the calculated phase gives a minimum detectable phase shift of $3\sigma = 3.9 \cdot 10^{-4}$ rad. For the normal interferometer with a sensitivity of 1530 rad/RIU this means the LOD is limited (for a bandwidth of 50 Hz) at $2.5 \cdot 10^{-7}$ RIU by electronic noise. The long interferometer of 13 000 rad/RIU would be limited at $3.0 \cdot 10^{-8}$ RIU. As the length difference of the MZI is increased the speed with which fringes pass by will also get higher requiring a higher detection bandwidth to keep up with the phase and thus slightly more electronic noise.

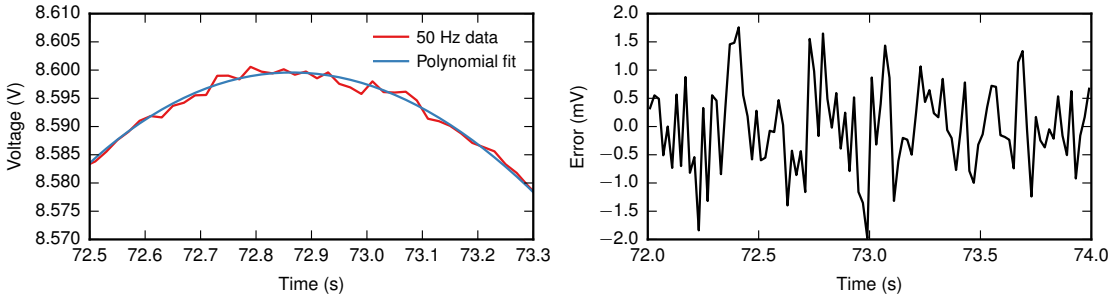

Figure 4.10: (a) Transition data downsampled to 50 Hz and a fifth order polynomial fit. (b) The difference between the polynomial fit and the data giving an indication of the noise level in the signal.

4.2.4 Interferometer non-linearity

Of more concern is variation in the amplitude of the three signals, causing non-linearity in the sensor response. A maximum variation of about 5% is observed, which is much higher than the photodetector noise level. A repeated measurement of a transition from demiwater to 12% salt solution shows that the variations do not change, which means they are not caused by temperature fluctuations during a measurement.

Another phenomena that can occur is roughness-induced backscattering by the waveguides [36]. The etching process that is used to remove silicon that is not part of the waveguide results in fairly random variations of the waveguide width (figure 4.11a), causing small reflections at many positions. In order to assess this, wavelength sweeps of straight and curved waveguides were carried out with the data in the frequency domain shown in figure 4.11b. For the x-axis the FSR is converted to an equivalent Fabry-Perot cavity length using formula 2.11 and an n_g of 4.5. The highest peak in both spectra clearly corresponds to the waveguide length. The higher power level left of the main peak is believed to be caused by the many small cavities resulting from reflections due to waveguide roughness. None of these cavities can be longer than the waveguide itself, which is why

the power drops off after the main peak. This fairly constant spectrum left of the peak contains both low and high frequencies and results in an irregular modulation of the intensity which could explain the lack of a pattern in the observed fringe amplitude variations.

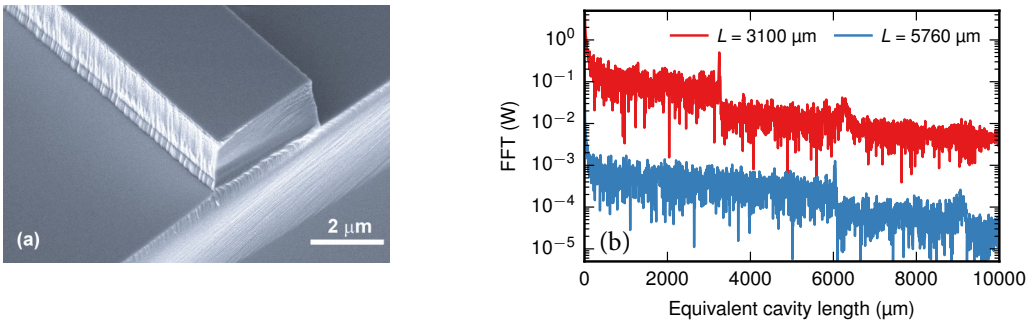

Figure 4.11: (a) Scanning electron microscope (SEM) micrograph of an SOI waveguide [37]. Visible is the sidewall roughness and almost perfectly flat top. (b) FFT of two wavelength sweeps of test waveguides. The drop in power at an equivalent cavity length equal to the waveguide length can be seen as evidence for backscattering. The red curve is offset by a factor 100 for clarity.

Also found in [36] is that the backscattered power is two orders of magnitude lower for TM than for TE polarized light. This can be explained by the TM mode profile of a single-mode SOI waveguide (figure 2.2) having much less interaction with the sides of the waveguide and instead more with the nearly flat top. If backscattering is the cause of fringe amplitude variation then using TM light could be a possible solution as all measurements have been carried out with TE light due to the grating couplers being optimized for this polarization. In addition to this, a TM mode results in a higher sensitivity since more mode power is present in the sensing region. Unfortunately no TM three-port MZI's or straight waveguides were available to test this hypothesis since the TM grating couplers were not working for unknown reasons.

In conclusion, the three-port MZIs already show high sensitivities and LODs similar to that of the ring resonator on the same chip. Photodetector measurements result in a phase resolution that in combination with the sensitivity of the long MZI can result in a state of the art LOD of $2.76 \cdot 10^{-8}$ RIU. A drawback compared to ring resonators is the non-linearity in the calculated phase caused by varying fringe amplitudes. It seems, however, that this can be strongly reduced by using TM instead of TE polarization.

5 Displacement sensing results

First, the interferometer signals due to displacement of the mirror in a previously performed experiment is shown in figure 5.1 for comparison.

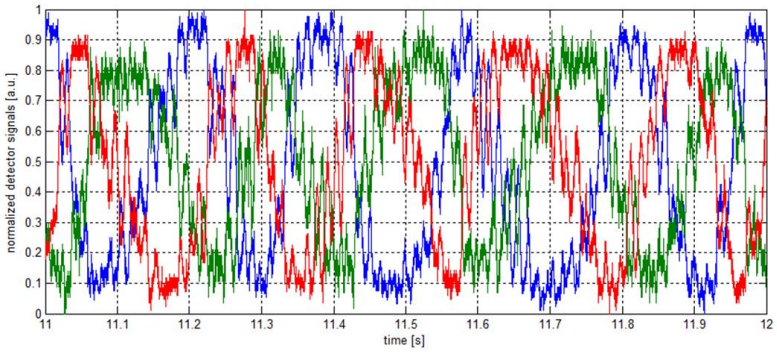

Figure 5.1: Results of previous experiments with this chip where the fiber between the chip and mirror was 3 mlong , causing wavelength noise of the laser to have a large effect on the interferometer signals.

After successful alignment of the setup (section 3.4.3), a wavelength sweep with a tunable laser was performed to evaluate the wavelength dependence of the photonic circuit. A small selection of the measurement is visible in figure 5.2. The FSR is very small because of the large effective length difference between the 3×3 interferometer arms of about 45 cm. Voltage V_1 of the photodiode before the 2×2 MMI coupler displays a significant pattern and appears to not only be modulated in intensity but also offset, excluding the possibility of it being merely the result of a Fabry-Perot cavity. It is thought that 2×2 MMI coupler might be sensitive to the polarization direction of the input light, but more investigation is needed. For further measurements with a constant wavelength 1550.0 nm was chosen since the amplitude of V_1 is reasonable at this point.

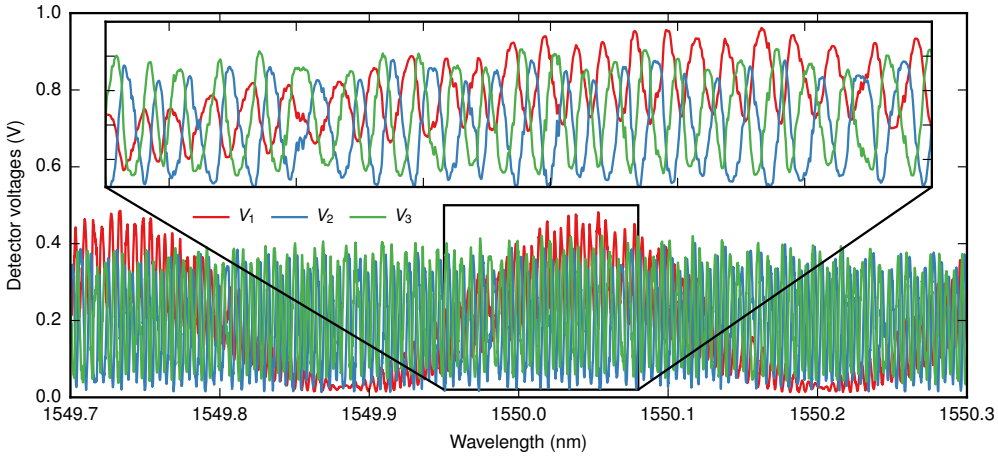

Figure 5.2: Wavelength sweep of the displacement 3×3 interferometer. In the inset a zoomed-in part of the measurement is shown.

The function generator driving the piezo-actuated mirror stage was set to a sine pattern of frequency 10 Hz and peak-to-peak amplitude of 5.67 V. Both the raw signals, normalized signals, and calculated displacement are shown in figure 5.3. From the normalized signals a deviation from the theoretical 120° phase differences can be clearly seen. A significant improvement of the noise level present in the interferometer signals can be observed when comparing figure 5.1 and 5.3, as was expected to be the case for a much shorter distance between the chip and mirror.

On the far left of the normalized signals in figure 5.3 correlation of the noise in the signals V_1 and V_2 can be clearly seen. Such correlations between signals can only be caused by either wavelength noise or changes in the optical path length, and for the latter the sensor is just measuring displacement as it should be. The wavelength-induced noise is reduced by a factor of 20 between the setup in figures 5.1 and 5.3 because of the shorter optical path.

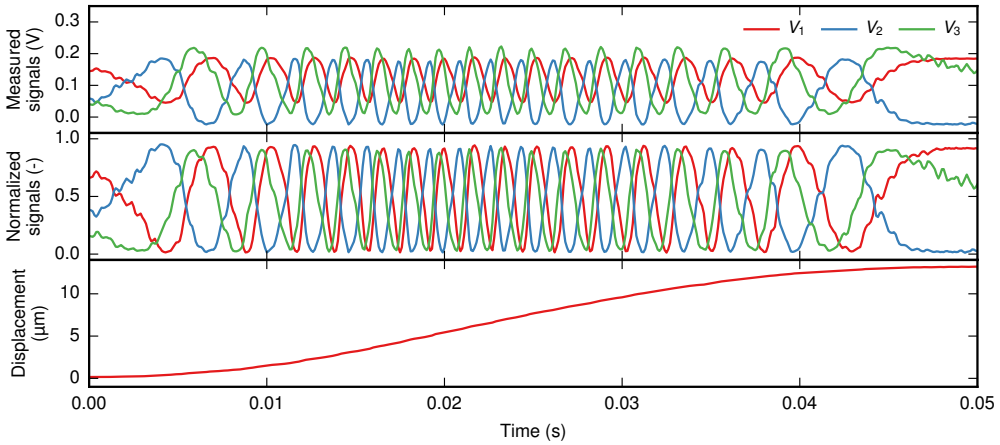

Figure 5.3: Signals during half a period of mirror movement. (Top) Raw amplified photodiode voltages. (Middle) Normalized photodiode voltages. (Bottom) Calculated phase from (Middle) converted to a displacement using the wavelength of 1550.0 nm.

To explore the influence of wavelength noise on the interferometer signals, two measurements of slow sinusoidal mirror movement were performed with two different light sources, as in figure 5.4. The measurement with a Thorlabs wavelength division multiplexing (WDM) source can be seen to exhibit a lower noise than that with the tunable laser source. However, the WDM measurement also shows more distorted fringes compared to the TLS measurement.

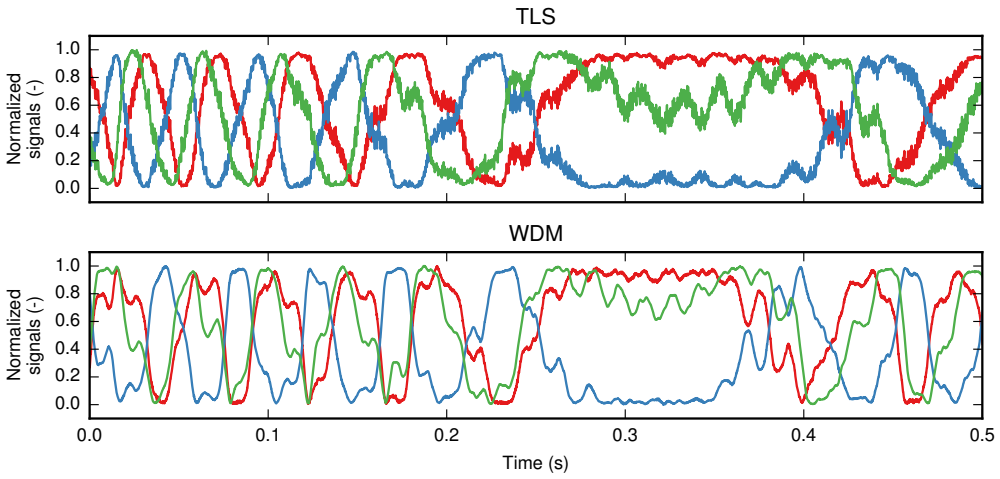

Figure 5.4: Interferometer signals during movement of the mirror with a TLS (Top) and WDM source (Bottom).

In order to evaluate the accuracy of the calculated displacement, the voltage applied with the function generator is converted to a displacement using the specified ratio of 20 µm per 10 V. The results in figure 5.5b show that the calculated displacement is significantly higher than that according to the function generator signal. An additional test in figure 5.5a where the piezo is adjusted through its full range results in a range of 24.5 µm which agrees with the larger displacement observed in figure 5.5b. An additional blue curve is plotted using a ratio of 24.5 µm per 10 V and shows good agreement when compared to the green curve for increasing displacement. Near the peak and for decreasing displacement however the curves do not correspond well any more. This is more likely to be caused by a combination of non-linearity and hysteresis of the piezo in the stage itself.

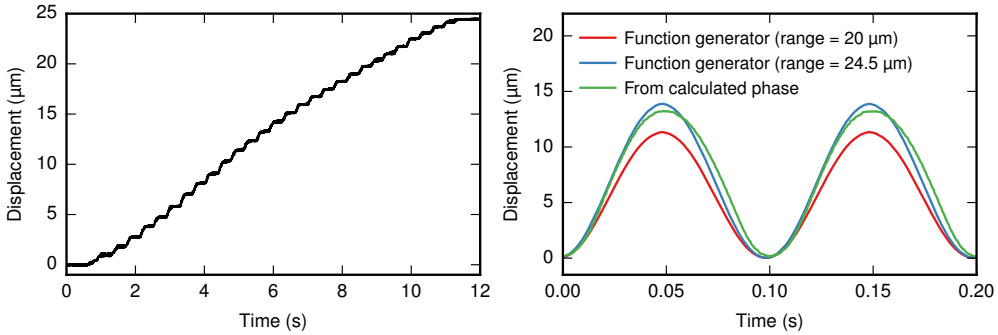

Figure 5.5: (a) Displacement calculated from the three signals during a manual adjustment through the full piezo range. (b) Displacement from both the interferometer and function generator. In blue the range found in (a) is used.

Looking in more detail at the displacement as for the blue curve in figure 5.6, slight bumps are observed. Plotting the displacement together with one of the interferometer outputs it is clear that the signals are correlated. In fact, this is a typical example of what happens when the phase is calculated using formula 2.16 while there is an offset in the phase shift of 120°. Calculating the phase with formula 2.17 and using $\theta_2 = 180°$ and $\theta_3 = 300°$ yields the red curve in figure 5.6 where the periodic effect is significantly reduced.

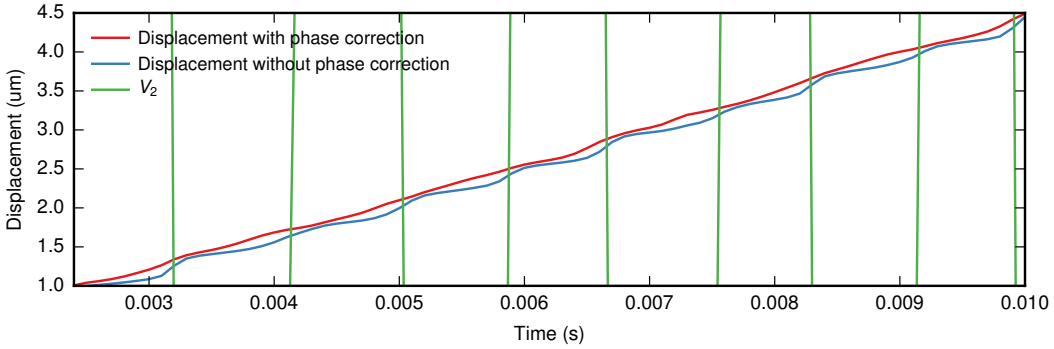

Figure 5.6: Plotting the displacement calculated from the phase against one of the interferometer signals reveals the cause of the periodic effect. V_2 has been scaled up significantly for illustration purposes and does not correspond to the units of the y-axis.

To summarize, an on-chip 3×3 interferometer has been successfully demonstrated for usage as a displacement sensor and the noise level was greatly reduced compared to previous experiments. It is difficult to attribute a detection limit to this sensor as the noise in the measured displacement is now primarily caused by vibrations of components in the setup itself. A way forward would be to characterize the setup in a vibration isolated environment, which the current lab was not. In contrast to the biosensor using a 3×3 interferometer of which the sensitivity can be increased with the arm length difference or sensing window length, the sensitivity of this displacement sensor is dependent on the wavelength that is used. In this case, the only figure to improve upon is the phase resolution.

6 Conclusion

Ring resonators and three-port Mach-Zehnder interferometer structures were compared for usage in refractive index sensing on a silicon-on-insulator platform. A three-port MZI offers high-bandwidth interrogation at a constant sensitivity that can be further increased by altering the arm length. Theoretical and experimental results indicate a sensitivity that scales linearly with the arm length difference. This, however, means that the chip footprint of a three-port MZI is larger than a ring resonator, and that ring resonators might be more suitable in applications where a large number of analytes must be detected simultaneously.

For the three-port MZIs, measurements with an external photodetector show that state of the art detection limits can be reached when photodetectors are either integrated on-chip or used externally. Temperature compensation can be realized by making use of equal MZI arms with a sensing window above one of them. A drawback is non-linearity in the calculated phase that is brought about by varying amplitudes of the interference fringes, which are thought to be caused by a combination of cavities created by roughness-induced backscattering of the waveguides and reflections of the vertical grating couplers. These effects can be reduced by optimizing the devices for TM polarization, which in turn also provides a higher sensitivity. The results altogether show that a three-port MZI is a promising device for high-sensitivity on-chip sensing applications such as pressure sensing, gas sensing, and biosensing.

If this project were to be continued, the recommendation would be to fabricate a three-port MZI with equal arms of length in the order of 1 cm for sufficient sensitivity, integrated photodiodes, and components optimized for TM polarization. Finally, actual bio or gas sensing experiments would have to be performed to demonstrate the detection of clinically relevant concentrations.

As for the integrated three-port MZI displacement sensor, a significant reduction of the noise due to wavelength fluctuations was achieved compared to a previous experiment by shortening the distance between the chip and mirror by a factor 20. Noise in the interferometer signals is now primarily due to vibrations on the optical setup itself. In order to properly assess the detection limit of this device, measurements in a vibration isolated environment need to be carried out.

Bibliography

[1] A. A. Michelson and E. W. Morley. "On the Relative Motion of the Earth and of the Luminiferous Ether". In: *Sidereal Messenger, vol. 6, pp. 306-310* 6 (1887), pp. 306–310.

[2] A. Einstein and Others. "On the electrodynamics of moving bodies". In: *Annalen der Physik* 17.10 (1905), pp. 891–921.

[3] A. Einstein. "Die feldgleichungen der gravitation". In: *Sitzungsberichte der Königlich Preußischen Akademie der Wissenschaften (Berlin), Seite 844-847.* (1915).

[4] B. P. Abbott et al. "Observation of gravitational waves from a binary black hole merger". In: *Physical review letters* 116.6 (2016), p. 61102.

[5] K. C. Kao and G. A. Hockham. "Dielectric-fibre surface waveguides for optical frequencies". In: *Electrical Engineers, Proceedings of the Institution of* 113.7 (1966), pp. 1151–1158.

[6] K Lawniczuk, M. K. Smit, and K. A. Williams. "ASPICs: Application Specific Photonic Integrated Circuits". In: *Photonics magazine* (2014), pp. 5–9.

[7] *ePIXfab: The silicon photonics platform*. (Visited on 02/07/2016).

[8] B. Drapp et al. "Integrated optical Mach-Zehnder interferometers as simazine immunoprobes". In: *Sensors and Actuators B: Chemical* 38-39 (1997), pp. 277–282.

[9] R. G. Heideman. "Chemical Remote opto-chemical sensing with extreme sensitivity : design , fabrication and performance of a pigtailed integrated optical phase- modulated Mach-Zehnder interferometer system". In: *Sensors and Actuators B* (1999), pp. 1–6.

[10] F. Prieto et al. "Integrated Optical Interferometric Biosensors based on Microelectronics Technology for Biosensing Applications". In: *Sensors and Actuators B chemical, Elsevier* 8 (2002), pp. 31–35.

[11] A. Densmore et al. "Silicon photonic wire biosensor array for multiplexed real-time and label-free molecular detection." In: *Optics letters* 34.23 (2009), pp. 3598–3600.

[12] D. Sarkar et al. "Optical biosensors with an integrated Mach-Zehnder Interferometer for detection of Listeria monocytogenes". In: *Biomedical Microdevices* 16.4 (2014), pp. 509–520.

[13] T. Chalyan et al. "Asymmetric Mach-Zehnder Interferometer Based Biosensors for Aflatoxin M1 Detection." In: *Biosensors* 6.1 (2016), pp. 1–10.

[14] S. Dante et al. "All-optical phase modulation for integrated interferometric biosensors". In: *Optics Express* 20.7 (2012), p. 7195.

[15] B. J. Luff et al. "Integrated Optical Mach fb Zehnder Biosensor". In: *Journal of Lightwave Technology* 16.4 (1998), pp. 583–592.

[16] P. Hua et al. "Integrated optical dual Mach-Zehnder interferometer sensor". In: *Sensors and Actuators, B: Chemical* 87.2 (2002), pp. 250–257.

[17] E. Kleijn et al. "Amplitude and phase error correction algorithm for 3x3 MMI based Mach-Zehnder interferometers". In: *Journal of Lightwave Technology* 33.11 (2015), pp. 2233–2239.

[18] K. De Vos et al. "Multiplexed antibody detection with an array of silicon-on-insulator microring resonators". In: *IEEE Photonics Journal* 1.4 (2009), pp. 225–235.

[19] M. Iqbal et al. "Label-free biosensor arrays based on silicon ring resonators and high-speed optical scanning instrumentation". In: *IEEE Journal on Selected Topics in Quantum Electronics* 16.3 (2010), pp. 654–661.

[20] D. Ullien et al. "Protein detection on biotin-derivatized polyallylamine by optical microring resonators." In: *Optics express* 22.13 (2014), pp. 16585–94.

[21] S. M. C. Abdulla et al. "Sensing platform based on micro-ring resonator and on-chip reference sensors in SOI". In: *Proceedings of SPIE* 8990 (2014), pp. 1–6.

[22] P. J. Harmsma et al. "'Click & Measure' optical interfacing to Silicon-On-Insulator chips". In: ().

[23] F Biesboer. "Trillingsvrije tafel". In: *De Ingenieur* (2010), pp. 16–17.

[24] S. O. Kasap. *Optoelectronics & Photonics: Principles & Practices*. Internatio. Pearson Highed Ed., 2013.

[25] *Apodized waveguide-to-fiber surface grating couplers*. 2013. URL: https://www.kth.se/en/ees/omskolan/organisation/avdelningar/mst/research/optics/apodized-waveguide-to-fiber-surface-grating-couplers (visited on 04/15/2016).

[26] F. Van Laere et al. "Compact and highly efficient grating couplers between optical fiber and nanophotonic waveguides". In: *Journal of Lightwave Technology*. Vol. 25. 1. 2007, pp. 151–156.

[27] B. Snyder and P. O'Brien. "Packaging process for grating-coupled silicon photonic waveguides using angle-polished fibers". In: *IEEE Transactions on Components, Packaging and Manufacturing Technology* 3.6 (2013), pp. 954–959.

[28] G. T. Reed and A. P. Knights. *Silicon photonics*. Wiley Online Library, 2008.

[29] L. B. Soldano and E. C. M. Pennings. "Optical Multi-Mode Interference Devices Based on Self-Imaging: Principles and Applications". In: *Journal of Lightwave Technology* 13.4 (1995), pp. 615–627.

[30] A. Yariv. "Critical coupling and its control in optical waveguide-ring resonator systems". In: *IEEE Photonics Technology Letters* 14.4 (2002), pp. 2001–2003.

[31] F. Pedrotti, L. Pedrotti, and L. Pedrotti. *Introduction to Optics*. Pearson Education Limited, 2014.

[32] M. Todd, G. Johnson, and B. Althouse. "A novel Bragg grating sensor interrogation system utilizing a scanning filter, a Mach-Zehnder interferometer and a 3x3 coupler". In: *Measurement Science and Technology* 12.7 (2001), pp. 771–777.

[33] M. Todd, M. Seaver, and F. Bucholtz. "Improved, operationally-passive interferometric demodulation method using 3x3 coupler". In: *Electronics Letters* 38.15 (2002), pp. 784–786.

[34] R. Halir et al. "Direct and sensitive phase readout for integrated waveguide sensors". In: *IEEE Photonics Journal* 5.4 (2013).

[35] J. E. Saunders et al. "Refractive indices of common solvents and solutions at 1550 nm". In: *Applied Optics* 55.4 (2016).

[36] F. Morichetti et al. "Roughness induced backscattering in optical silicon waveguides". In: *Physical Review Letters* 104.3 (2010), pp. 1–4.

[37] Q. Xia et al. "Ultrafast and selective reduction of sidewall roughness in silicon waveguides using self-perfection by liquefaction". In: *Nanotechnology* 20.34 (2009), p. 345302.

Appendix A: Project description

Characterization of novel integrated photonics biosensor

(Physics /optics master student, 6-9 month)

TNO has developed a nano-photonic biosensor that could be employed in point-of-care diagnostics applications (lab-on-a-chip). The biosensor consists of a waveguide-based interferometer integrated on a Silicon-on-Insulator optical IC. One of the branches of the interferometer can be functionalized with antibodies against a biomarker (typically a protein). Once a patient sample is applied to the sensor, the biomarker will bind to the antibodies resulting in a local change in refractive index. Interaction of the surface-bound biomarkers with the evanescent field extending from the waveguide leads to a phase change detected using the interferometer. The biosensor has been fabricated and currently needs to be characterized in order to determine its performance. Moreover, recommendation for improvement need to be given. The assignment consists of:

1. Development of set-up to (optically) interface with chip.
2. Development of SW (could be matlab script) to process sensor signals (real-time or off-line).
3. Measurement of performance of chip in term of ambient refractive index sensitivity, temperature sensitivity, limit of detection and exploration of what is limiting the performance. If time permits actual protein detection experiments can be performed.
4. Writing a report discussing the results of the research and potentially publish the results in a scientific journal.

Appendix B: Phase calculation and error propagation

We start with three ideal positive cosines shifted 120 degrees relative to each other given by

$$x = \frac{A}{2}(1 + \cos(\phi)) \qquad y = \frac{A}{2}(1 + \cos(\phi + 120^\circ)) \qquad z = \frac{A}{2}(1 + \cos(\phi + 240^\circ)).$$

Using a trigonometric identity the signals with phase shifts are rewritten into

$$y = \frac{A}{2}(1 + \cos(\phi)\cos(120^\circ) + \sin(\phi)\sin(120^\circ)) = \frac{A}{2}\left(1 - \frac{1}{2}\cos(\phi) + \frac{\sqrt{3}}{2}\sin(\phi)\right)$$
$$z = \frac{A}{2}(1 + \cos(\phi)\cos(240^\circ) + \sin(\phi)\sin(240^\circ)) = \frac{A}{2}\left(1 - \frac{1}{2}\cos(\phi) - \frac{\sqrt{3}}{2}\sin(\phi)\right).$$

From a combination of y and z

$$y - z = \frac{\sqrt{3}}{2}A\sin\phi \qquad \text{or} \qquad \sin\phi = \frac{2}{A\sqrt{3}}(y - z) \tag{6.1}$$

results and from a combination of all three signals

$$2x - y - z = \frac{3}{2}A\cos\phi \qquad \text{or} \qquad \cos\phi = \frac{2}{3A}(2x - y - z) \tag{6.2}$$

results. Finally by dividing formula 6.1 by 6.2 a formula for calculating the phase independent of the signal amplitude is obtained. All signals must however be of equal amplitude.

$$\tan\phi = \frac{\sin\phi}{\cos\phi} = \sqrt{3}\frac{y - z}{2x - y - z} \tag{6.3}$$

In order to see how measurement uncertainty in the individual signals affects the calculated phase a formula for the error propagation is derived. We start with formula 6.3 written for the phase as

$$\phi = \arctan\left(\sqrt{3}\frac{y - z}{2x - y - z}\right) \tag{6.4}$$

and the general formula for propagation of uncertainty

$$\sigma_\phi = \sqrt{\left(\frac{\partial\phi}{\partial x}\right)^2\sigma_x^2 + \left(\frac{\partial\phi}{\partial y}\right)^2\sigma_y^2 + \left(\frac{\partial\phi}{\partial z}\right)^2\sigma_z^2}. \tag{6.5}$$

The three partial derivatives are found to be

$$\frac{\partial\phi}{\partial x} = \frac{2\sqrt{3}(z - y)}{3(y - z)^2 + (y + z - 2x)^2}$$
$$\frac{\partial\phi}{\partial y} = \frac{2\sqrt{3}(x - z)}{3(y - z)^2 + (y + z - 2x)^2}$$
$$\frac{\partial\phi}{\partial z} = \frac{2\sqrt{3}(y - x)}{3(y - z)^2 + (y + z - 2x)^2}$$

and because of the symmetry can be written in the following form using formula 6.5 for the uncertainty in the phase

$$\sigma_\phi = \sqrt{12\frac{(z - y)^2\sigma_x^2 + (x - z)^2\sigma_y^2 + (y - x)^2\sigma_z^2}{[3(y - z)^2 + (y + z - 2x)^2]^2}}. \tag{6.6}$$

Appendix C: Infrared camera non-linearity calibration

Because the interferometer signals from the first measurements were showing small deformations when compared to an ideal sinusoid, a linearity calibration of the IR camera was carried out. In order to do this the tunable laser source was set at a constant wavelength and power. Its output is connected to a variable attenuator and then split in two, with one half of the power passed to an optical power meter and the other half through a polarization controller to the chip. On the chip a straight test waveguide was used instead of the three port interferometer to provide a constant signal power. The light coming from the output grating coupler of this waveguide is then measured using the IR camera.

In order to measure the linearity of the camera the maximum pixel values are measured while changing the applied optical power with the variable fiber attenuator. The results in figure 6.1a show a relatively high degree of non-linearity in the pixel values, explaining the deformations in the measured signals at pixel counts around $2 \cdot 10^2$ and 10^3 as the linearity changes. Using this information a correction curve is made, as shown in figure 6.1b, where a mapping is created from measured pixel values to corrected ones that change linearly with optical power.

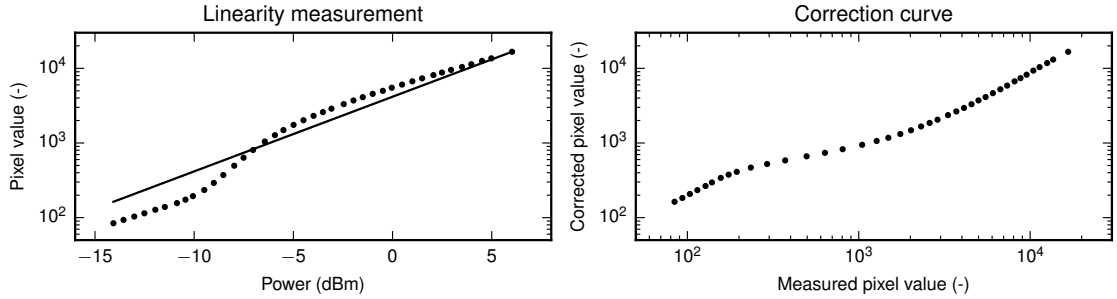

Figure 6.1: (a) Measured maximum pixel values in the camera image as a function of the optical power. The line represents the linear relation between the pixel value at zero optical power (not shown in log scale) and the value near camera saturation. (b) By calculating the expected pixel value from the linear relationship in (a) corresponding to the measured pixel value a mapping function is obtained.

Refractive Index Sensing Using a Three-Port Interferometer and Comparison With Ring Resonators

Ruben J. J. van Gulik, Bart M. de Boer, and Peter J. Harmsma

***Abstract*—In this paper, we compare ring resonator and three-port Mach-Zehnder Interferometer (MZI) devices fabricated on Silicon-On-Insulator for the purpose of refractive index sensing. Their respective sensitivities and Limits Of Detection (LOD) were determined with NaCl solutions. A sensitivity of 113.07 nm per Refractive Index Unit (RIU) and LOD of 2.47×10^{-6} RIU was reached for the ring resonators. The most sensitive three-port MZI has a sensitivity of 13 051 rad/RIU, and an LOD of 2.76×10^{-8} RIU is shown to be attainable. A three-port MZI combines several advantages of both ring resonators and normal MZI devices, including a constant and scalable sensitivity, high-bandwidth read-out, no directional ambiguity, and a simple interrogation setup. Such a device is promising for applications like pressure, gas, and biosensing.**

***Index Terms*—Ring resonator, three-port Mach-Zehnder interferometer, refractive index sensing, biosensor, integrated photonics.**

I. Introduction

In the last decade silicon photonics has grown into a mature technology, where many foundries offer high quality and reliable processes in different material systems such as Indium Phosphide, Silicon-On-Insulator (SOI) and dielectric waveguides. Traditionally, silicon photonics has been employed for applications in telecommunication, such as modulators and switches [1]. However, increasingly silicon photonics is employed in the area of photonic sensing. The technology has been shown to be a promising platform for on-chip sensors for various applications, owing among others to the use of existing processes that are well known from semiconductor manufacturing, which results in low per-device costs for high-volume production. Therefore, the devices can be considered as disposables. In addition, high sensitivities are consistently reached. As silicon photonic sensors typically have a very small footprint, many sensors can be integrated on a small silicon area allowing multi-functional devices.

Sensors have been developed for ultrasound [2], pressure sensing [3], gas sensing [4] and biosensing [5]–[12]. In the area of photonic biosensing, ring resonators [5]–[9], photonic crystals [10] and different interferometer devices such as Mach-Zehnder Interferometers (MZI) [11] and Young Interferometers [12] are commonly used to detect analytes in aqueous solutions. These applications typically rely on the sensors ability to detect minute changes in the ambient refractive index. As for biosensors, the binding of analytes to receptors immobilized on the device surface results in this refractive index change, leading to a measurable optical response of the sensors.

Biosensors based on MZIs have been demonstrated to reach high sensitivities, but their read-out is troubled by fading of the sensitivity near the fringe extremes. Modulation schemes have been developed to avoid this problem [13] at the cost of complicating the device and signal processing. A three-port 3×3 MZI provides three outputs at a 120° mutual phase difference, avoiding sensitivity fading. Three-port MZIs have been developed using directional couplers to create the 120° phase differences [14], [15], or using 3×3 Multi Mode Interference (MMI) couplers [16].

In this paper, a comparison is made between two distinct types of sensors, namely ring resonator sensors and 3×3 MZI sensors, fabricated in SOI and located on the same chip. More specifically, their use as an ambient refractive index sensor has been investigated. The 3×3 MZI uses a 3×3 MMI coupler to provide the outputs. The focus has been on exploring the different advantages and disadvantages that these sensors have, related to potential sensing applications

II. Theory

The principle on which both ring resonator and interferometer based photonic sensors rely are changes of the effective refractive index n_{eff} of the waveguide mode due to changes in the ambient refractive index n_{ambient} via the evanescent field interaction

$$\Delta n_{\mathrm{eff}} = \frac{\partial n_{\mathrm{eff}}}{\partial n_{\mathrm{ambient}}} \Delta n_{\mathrm{ambient}} \tag{1}$$

where the partial derivative depends on parameters such as the wavelength and waveguide geometry. This derivative is often assumed to be equal to the confinement factor Γ given by the ratio of power in the ambient material relative to the total power, but simulations with mode solving software (FIMMWAVE [17]) for the applied waveguide geometry result in a 50% higher sensitivity than predicted by the confinement factor.

A. Ring Resonator

Light can be coupled into a circular waveguide with circumference L using either directional couplers or MMI couplers (Figure 1b). When this light travels around the ring multiple times it will interfere with input light, and with light that has

Ruben J. J. van Gulik, Bart M. de Boer, and Peter J. Harmsma are with TNO, Stieltjesweg 1, 2628 CK Delft, The Netherlands (e-mail: peter.harmsma@tno.nl).

Manuscript received -; revised -.

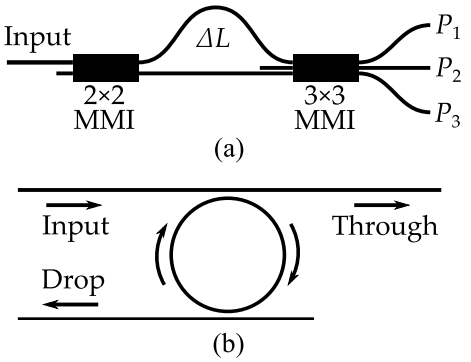

Fig. 1. Schematical representation of the sensing structures compared in this paper. (a) Three-port MZI with an arm length difference. (b) Ring resonator with through- and drop-port.

been previously coupled into the ring. A resonating condition will occur for wavelengths that fit an integer amount of times in the circumference L because of constructive interference. These resonance wavelengths λ_{res} are given by

$$\lambda_{\mathrm{res}} = \frac{L n_{\mathrm{eff}}(\lambda_{\mathrm{res}})}{m} \tag{2}$$

in which m is an integer called the mode number. Ring resonators can be interrogated by measuring either the output of the same waveguide that is used for the in-coupling of light, or the output of a separate second waveguide coupled to the same ring. These are called the 'through' and 'drop' ports, respectively, and exhibit either notches or peaks in the transmission spectrum. Taking dispersion into account, the shift in resonant wavelengths as a result of a change in n_{ambient} is

$$\Delta\lambda_{\mathrm{res}} = \frac{\lambda_{\mathrm{res}}}{n_g(\lambda_{\mathrm{res}})}\Delta n_{\mathrm{eff}} \tag{3}$$

where n_g is the group index and the Δn_{eff} is given by Equation 1. One particular method of interrogating a ring resonator is to measure its transmission spectrum within a fixed wavelength range with a tunable laser source, and to identify the location of the resonance wavelength(s) in this spectrum. By repeating this procedure at regular intervals, the resonance shift over time can be obtained. It is clear that one of the primary factors to limit the precision of such a system is the resolution of the wavelength-tunable input light source that is used. Temperature-induced drift of the resonant wavelengths can be corrected for by means of a second identical ring covered by a protective layer. An additional important parameter is the free spectral range (FSR) which is the spacing in wavelength between resonances

$$(\Delta\lambda)_{\mathrm{FSR}} = \frac{\lambda^2}{n_g L}. \tag{4}$$

Experimental conditions must be such that successive spectra do not shift by more than half an FSR, because in that case the actual shift may be the observed shift plus or minus an integer times the FSR.

The Extinction Ratio (ER) of the ring response is the ratio between maximum and minimum transmission, and the Q-factor a measure for the spectral width of the resonances.

TABLE I
COMPARISON OF THE THREE SENSING STRUCTURES DISCUSSED IN THIS PAPER FOR SEVERAL PROPERTIES.

	Ring resonator	Normal MZI	3×3 MZI
Linearity	✓✓✓	✓✓	✓✓
Multiplexability	✓✓✓	✓	✓
Ease of read-out	✓	✓✓	✓✓✓
Read-out bandwidth	✓	✓✓✓	✓✓✓
Footprint	✓✓✓	✓✓	✓✓
Directional ambiguity	✓✓✓	✓	✓✓✓
Source wavelength	Tunable	Fixed	Fixed
Sensitivity	Waveguide geometry	Arm length, zero at peaks	Arm length

Both the ER and Q-factor depend on the waveguide-to-ring coupling coefficient and round-trip transmission, with the sharpest resonances obtained when these factors are closest to unity and equal [18]. Sharper resonances are beneficial for obtaining a high wavelength accuracy.

B. Mach-Zehnder Interferometer

Using an MZI for sensing simplifies the read-out due to the fact that the input wavelength is kept constant, avoiding the need for an expensive tunable laser. An MZI for usage in biosensing is usually implemented with equal arm lengths, where one of the arms is covered by a protective layer. In such a configuration, the influence of temperature fluctuations is reduced since both arms will experience the same length and refractive index change. Alternatively, the arms have a length difference L and an increase in n_{eff} will induce a larger phase difference $\Delta\phi$ in the longer arm. For both configurations the phase difference can be expressed as

$$\Delta\phi = \frac{2\pi L \Delta n_{\mathrm{eff}}}{\lambda}. \tag{5}$$

where L stands for either the sensing window length or arm length difference for equal and unequal arms lengths, respectively. As is clear from Equation 5, the phase sensitivity scales with L allowing for high sensitivities. The primary disadvantages of such an MZI is that the derivative of the outputs with respect to phase change is zero at the fringe extremes. Consequently, at these extremes, the sensitivity is zero, and there is a directional ambiguity of the change in n_{eff}.

C. 3×3 Mach-Zehnder Interferometer

As opposed to a conventional 2×2 MZI, the 3×3 MZI combines both arms with a 3×3 coupler resulting in three outputs that have a mutual 120° phase difference (Figure 1a). The sum of the output powers at any phase is constant, providing a way of correcting for input power fluctuations. Assuming an ideal device, the individual signals can be described by

$$P_n = \frac{P_0}{3}\left[1 + V\sin\left(\Delta\phi + \frac{2\pi(n-1)}{3}\right)\right] \tag{6}$$

where P_n is the output power at output n, P_0 is the total input power, V the fringe visibility, $\Delta\phi$ the phase and $n = 1, 2, 3$.

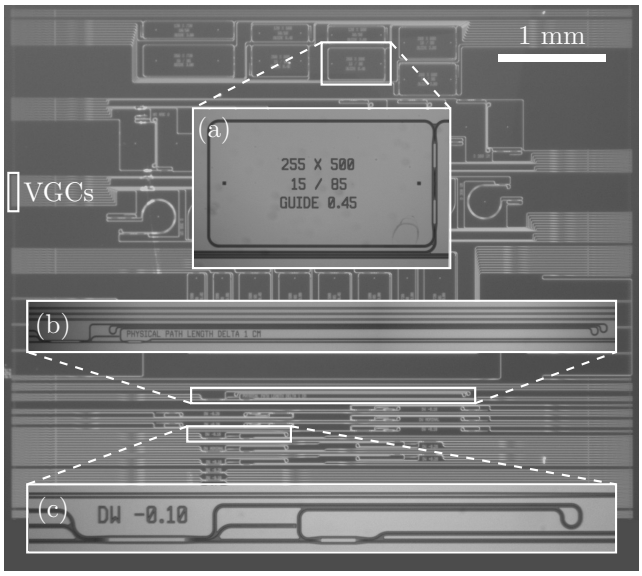

Fig. 2. Layout of the photonic chip. The VGCs are located on the far left and right sides to allow a flowcell to be placed in the middle. (a) The ring resonator with a circumference of 1825 µm. (b) The 3×3 MZI with a long arm difference of 9000 µm. (c) The 3×3 MZI with a shorter arm difference of 1050 µm. The two MMIs are clearly visible. The unused port of the 3x3 MMI is tapered to the minimum allowed width (120 nm), so that it becomes cut-off, and will not cause any unwanted reflections.

The equation contains three unknowns (P_0, V and $\Delta\phi$), and three values P_n so that each unknown can be solved for. Using equation 6 and assuming normalized signals, the obtained expression for ϕ has no directional ambiguity and nearly constant sensitivity:

$$\tan(\phi) = \sqrt{3}\frac{P_2 - P_3}{2P_1 - P_2 - P_3}. \tag{7}$$

D. Advantages and disadvantages

In Table I, the scores of ring resonator, normal MZI and 3×3 MZI sensing structures for various properties are listed for comparison. Ring resonators score high for multiplexability since the through-port of multiple rings can be read out with a single waveguide, resulting in superimposed transmission spectra. The read-out of ring resonators is, however, more complex than for the interferometers since wavelength sweeps have to be carried out resulting in lower bandwidths and more signal processing. The footprint of a three-port MZI could be a slight drawback since it scales with the sensitivity.

III. Experimental Details

A. Photonic Circuit

A chip, shown in Figure 2, was designed and fabricated by making use of the ePIXfab silicon photonics platform [19]. The waveguides are 450 nm wide and 220 nm thick, providing single-mode operation for both TE and TM polarizations at a wavelength around 1550 nm, and waveguide losses in the order of 3 dB/cm. All optical in- and output is achieved using Vertical Grating Couplers (VGCs) which are optimized for TE polarization at an angle of 10° relative to the normal of the chip and result in coupling losses in the order of 6 dB. No integrated photodiodes have been used in this iteration in order to perform cost-effective testing, although these are readily available in the ePIXfab platform.

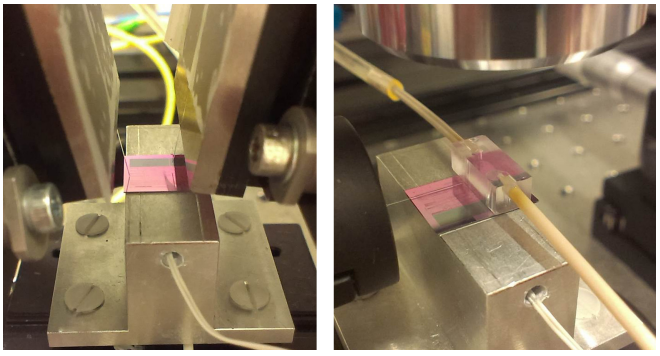

(a) (b)

Fig. 3. (a) Transmission measurements using two cleaved fibers tilted at 10°. (b) Read-out of the 3×3 MZI with an angle polished fiber on the left positioned above the chip and a microscope objective above the chip.

Ring resonators of different shapes, lengths and coupling mechanisms have been included on the chip. All rings can be interrogated by reading out the through port and some rings also contain an extra waveguide to be able to measure the drop port. For coupling between the ring and the bus waveguide, 2×2 MMI couplers with a length of 57.15 µm long and width of 6.9 µm were used. The use of MMIs as opposed to directional couplers provides reproducible coupling performance, highly robust against fabrication variations. MMIs provide a 50/50 or 15/85 split, so that only moderate Q-factors can be achieved. In a few devices in this work, the coupler is a small MZI interferometer composed of two MMIs. This MZI has a small arm length difference, so that arbitrary coupling ratios can be achieved. The device in Figure 2a shows such an interferometric coupler. We found that this concept results in only moderately improved Q-factors due to doubled MMI insertion losses. In current state-of-the-art SOI processing, the use of directional couplers allows reproducible fabrication of high Q-factor devices. In this work, the resonance width was sufficiently narrow to allow sub-pm read-out.

The 3×3 interferometers are composed of the same 2×2 MMI as used for the ring resonators, and a 3×3 MMI of 125 µm long and 7.2 µm wide. The waveguides connecting to the MMIs were tapered from 450 nm to 2.1 µm to reduce the effect of fabrication errors on the MMI performance and were offset by one third of the MMI width (2.4 µm). The length difference between the two arms is 1050 µm or 9000 µm, so that the devices can be tested as a refractive index sensor without the need for a protective layer on one of the arms, thus saving a processing step.

B. Salt Solutions and Fluidics

Solutions of 3, 6, 9 and 12% mass percentage NaCl corresponding to a range of 0.020 RIU were created for the measurements using de-ionized water and NaCl (31434, Sigma

Aldrich). The refractive indices of the solutions were calculated with an empirical formula that is valid for a wavelength range of 1530 to 1565 nm and NaCl mass percentages up to 25% [20]. All measurements were started with a de-ionized water baseline.

In order to flow liquids past the ring resonators and interferometers of the chip a flowcell was used that is attached to the chip with UV-cured Norland 61 optical adhesive. The flowcell was milled from polymethylmethacrylate (PMMA) and contains a channel at the bottom that was tapered to a width of 3 mm over a length of 1.5 mm and is 0.5 mm high and 7 mm long. A flowrate of 85 µL min^{-1} results in laminar flow and was used for all the measurements. One side of the flowcell was connected to an Aladdin AL1000-220 syringe pump which draws the liquid from a container holding the solution at the other side.

C. Optical Coupling and Read-Out

Spectral transmission measurements of the ring resonators and interferometers were carried out using a combination of an Agilent 81960A tunable laser source and an Agilent N7744A optical power meter. The laser has a wavelength resolution of 1 pm. Optical coupling to the chip was done using non-polarization maintaining fibers (Figure 3a), and a polarization controller was used to optimize the coupling to the TE-compatible VGCs.

During fluid measurements with the ring resonator, the input was excited with the mentioned tunable laser at a power of 6 mW and continuously swept between 1530 and 1540 nm in steps of 1 pm and a speed of 10 nm/s. Measuring the power at the through-port resulted in one transmission spectrum per second.

As for the interferometer fluid measurements, the three output VGCs are too closely spaced to be read out simultaneously with a fiber array. Therefore, a Xeva 1.7-640 IR camera with a framerate of 25 Hz and 14-bit pixel depth was used to measure the three outputs of the interferometers by imaging the output spots of the VGCs through a microscope system (Figure 3b). The integration time per frame is adjusted so that pixel saturation is almost reached for a maximum output power. In this case angle-polished fibers positioned parallel to the chip surface were used to couple light into the device, since the microscope objective occupies most of the space above the chip. These fibers are polished at an angle of 40° so that light reflects downward at an angle of 10° (as required by the VGCs) by total internal reflection [21].

To estimate the sensitivity in a representative situation where the outputs are monitored by means of photodetectors, additional measurements were done on a single 3×3 interferometer output using an external photodetector. In this case, two angle-polished fibers were aligned for optimal coupling and then fixed in place with UV-cured Norland 61 optical adhesive. This was done to eliminate modulations caused by the effect of vibrations on the fiber-to-chip coupling. The power is measured with a Thorlabs PDA10CS InGaAs detector.

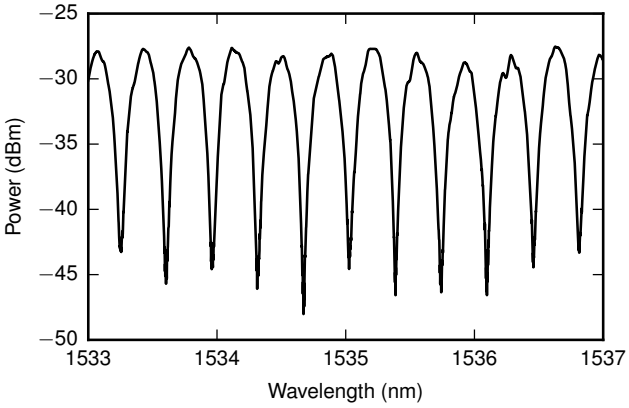

Fig. 4. Resonances in the transmission of the ring resonator showing an ER of more than 15 dB and FSR of 357 pm, conform to the design parameters.

D. Signal Processing

The ring resonator measurements were automated with custom software that controls the previously mentioned Agilent laser and detector combination. This application finds the wavelength shift of the resonances by performing a cross-correlation between the most recent and previous spectrum and sinc-interpolating the result to improve the wavelength resolution to 0.1 pm. The shifts between successive spectra are summed to obtain the resonance shift over time.

As for the interferometers, a recording with the IR camera is made of the VGC spots during a measurement. In order to extract the three signals, the frame is divided into three regions of interest and the maximum pixel value in each of these regions is determined for every frame. The signals are individually normalized using their respective minimum and maximum values. Further dividing by the sum of the signals at every point in time is done to correct for power fluctuations. A low-pass filter cut off at 1 Hz for the short interferometer and 3 Hz for the long variant is applied to improve the signal-to-noise ratio while taking care not to distort the fringes. Finally the phase is calculated using Equation 7 and unwrapped.

IV. Results and Discussion

A. Ring Resonator

The transmission spectrum of the tested ring resonator (Figure 2a) is shown in Figure 4. In the Fourier transform of the transmission spectra (shown only for the MZI in Figure 6, but the results are similar for both the ring resonators and MZIs), a peak corresponding to the device FSR is always clearly observed. In addition, spurious peaks appear at lower strength. One of these peaks corresponds to the Fabry-Perot cavity formed between the top side of the chip and the polished back side. In addition, higher-frequency peaks were observed, corresponding to Fabry-Perot cavities having an optical length equal to the distance between the input and output VGCs times the waveguide group index. Consequently, to obtain an optimum response, reflections at VGCs and at the chip bottom side should be minimized.

The results of a measurement where all salt solutions are applied successively every 10 minutes is shown in Figure 5.

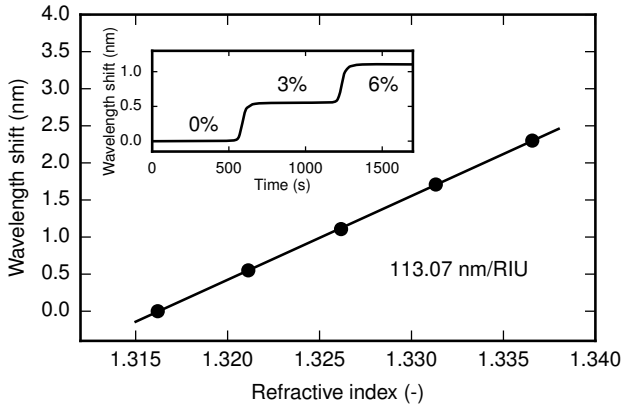

Fig. 5. Ring resonator resonance wavelength shifts starting with de-ionized water and successive 3, 6, 9 and 12% salinity solutions. In the inset the wavelength shift as a function of time during two changes in salinity is shown. Shifts in the main figure are obtained by averaging the data points in the plateaus of the inset figure. The sensitivity results from a good linear fit with the data.

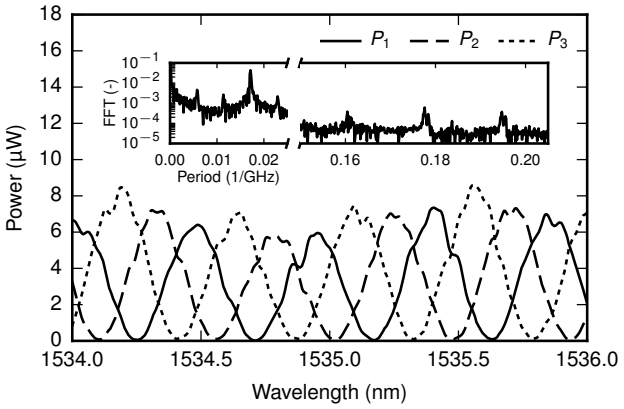

Fig. 6. The three output powers of the $\Delta L = 1050\,\mu\text{m}$ 3×3 MZI during a wavelength sweep. In the inset Fourier spectrum the low- and high-frequency modulations are further analyzed. The peak at $0.005\,\text{GHz}^{-1}$ corresponds to the substrate cavity, the strongest peak to the device FSR, and the peak at $0.18\,\text{GHz}^{-1}$ to the cavity formed by the VGCs.

This data set results in a sensitivity of 113.07 nm/RIU, which is comparable to what similar rings can achieve [8]. Due to the optimized analyis algorithm, the noise level in the wavelength shift was calculated to be only $3\sigma = 0.279\,\text{pm}$ which in combination with the sensitivity gives a Limit Of Detection (LOD) of 2.47×10^{-6} RIU.

B. 3×3 Interferometers

Similar initial wavelength sweeps were also carried out for both the short and long 3×3 interferometers. A representative sweep of the short interferometer (Figure 6) clearly shows low and high frequency modulations of the powers, again caused by reflections between the top and bottom side of the chip, and by reflections between the VGCs, respectively. When the 3x3 MZI is applied as a sensor, refractive index changes will also affect the length of the optical cavity between the VGCs, so that the high frequency modulations in Figure 6 will shift as well. This will have an impact on the relative output powers, and lead to non-optimal results. The slow envelope will stay stationary, since the optical thickness of the chip does not change, and the wavelength is fixed.

A part of the short interferometer measurement with the salt solutions at a constant wavelength of 1535 nm is shown in Figure 7. Fringes can clearly be seen at the transition between solutions. Small dips in the phase are observed just before the phase stabilizes at the new solution. These dips are most likely caused by some of the previous solution flowing back to the interferometer waveguides and temporarily lowering the refractive index.

The measurement with the long interferometer (Figure 8) shows an increase in the amount of fringes for a transition as is expected for the larger length difference. The fringe visibility however was not good allowing only the upper 12% of the pixel value range to be used which degraded the signal-to-noise ratio after normalization.

The phase shifts for both the short and long interferometer during the fluid measurements are visible in Figure 9. A

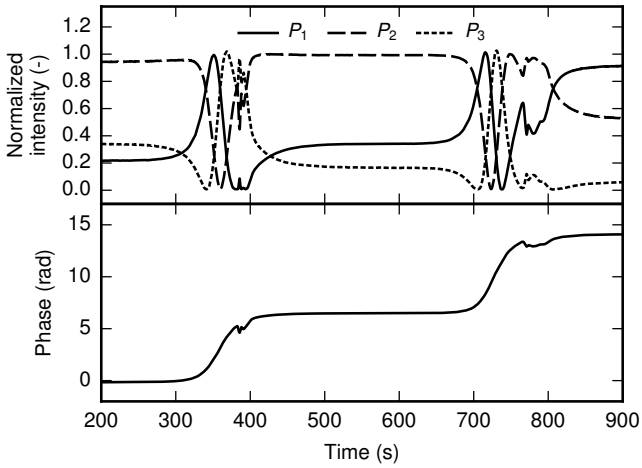

Fig. 7. Two changes of salinity measured with the short 3×3 interferometer. (Top) The three normalized individual signals. (Bottom) The phase calculated from the signals above.

linear fit results in a sensitivity of 1530 rad/RIU for the short interferometer and 13 051 rad/RIU for the long variant. The ratio 13051/1530 = 8.53 of the sensitivities corresponds to that of the path differences of 9000/1050 = 8.57 as is expected. Using Equations 1, 3, and 5, and the ring resonator sensitivity of 113.07 nm/RIU, an expected short interferometer sensitivity of 1396 rad/RIU was calculated. This corresponds to within 10% to the measured sensitivity of 1530 rad/RIU.

C. Short 3×3 Interferometer with External Photodetector

The signal of a single output of the short interferometer during a salt solution transition was measured with an external photodetector to assess the noise levels reachable with on-chip photodiodes as opposed to with an IR camera. A measurement during a transition from 0% to 6% salinity is shown in Figure 10, where the data was taken at a bandwidth of 200 kHz and low-pass filtered up to a frequency of 25 Hz, which is the frame rate of the IR camera. The Signal-To-Noise ratio is 1.15×10^4 at the peak in Figure 10, and is dominated by shot noise. By

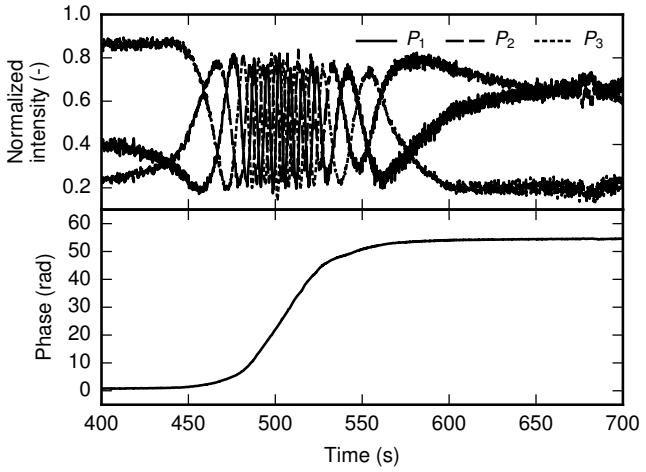

Fig. 8. A single change in salinity measured with the long 3×3 interferometer. Compared to figure 7 a roughly ninefold increase of fringes passes by.

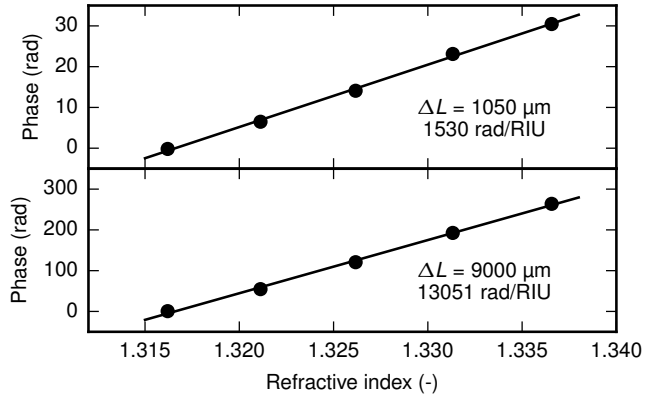

Fig. 9. Phase shifts starting with de-ionized water and successive 3, 6, 9 and 12% mass percentage NaCl solutions for the short (Top) and long (Bottom) 3×3 MZI.

using an error propagation model of Equation 7 and assuming the relative noise level scales with the square of the signal amplitude, the phase resolution is $3\sigma = 3.6 \times 10^{-4}$ rad, corresponding to LODs of 2.35×10^{-7} RIU and 2.76×10^{-8} RIU for the short and long 3×3 MZI, respectively.

D. Non-Linearity in the Calculated Phase

Using 3×3 interferometers as refractive index sensors can offer state-of-the-art LODs for integrated photonic sensors. To also achieve a good linearity, it is necessary to account for possible deviations from the ideal 120 phase shift, and to apply proper normalization. Blind calibration algorithms have been developed for this purpose [16], [22]. In addition, in Figures 7, 8 and 10 it is observed that the fringe amplitude shows some variation, degrading linearity when Equation 7 is directly applied. Fringe amplitude variation is attributed to spurious reflections and back scattering. Reflections can be minimized by proper design, backscattering by improved fabrication. The use of TM polarization will also result in smaller backscattering, and in improved sensitivity to ambient index.

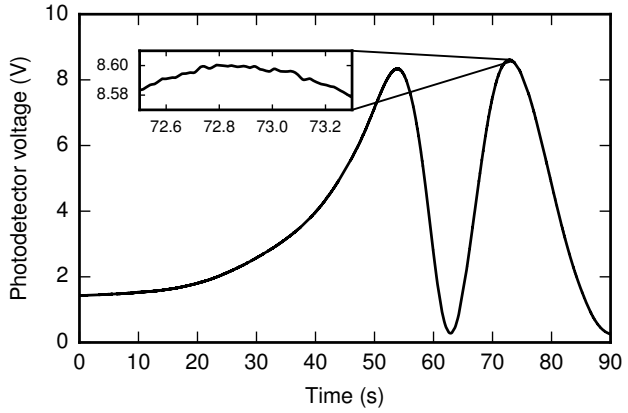

Fig. 10. The photodetector signal at a single output of the short interferometer during a transition from 0% to 6% salinity. In the inset a zoomed-in part of one of the fringe peaks is shown.

V. CONCLUSION

We compared ring resonators and three-port Mach-Zehnder interferometers for use in refractive index sensing on a silicon-on-insulator platform. A three-port MZI offers high speed interrogation at a constant sensitivity that can be further increased by altering the arm length. Theoretical and experimental results indicate a sensitivity that scales linearly with the arm length difference. State-of-the-art detection limits can be reached with external photodetectors, or with monolithically integrated photodiodes. Ring resonators offer the advantages of having a better linearity, and their multiplexability might make them more suitable for analysis of a large number of analytes at the same time. Improvements in linearity of the interferometer can be made by proper calibration of the actual phase differences of the MZI outputs, by advanced fabrication technology to reduce back scattering, and by proper design to minimize spurious reflections. The use of TM polarization can contribute to improvement in sensitivity due the higher evanescent field amplitude, and in linearity due to reduced back scattering. Our results show that a three-port MZI is a promising device for high-sensitivity on-chip sensing applications such as pressure, gas, and biosensing.

REFERENCES

[1] M. Pantouvaki, H. Yu, M. Rakowski, P. Christie, P. Verheyen, G. Lepage, N. Van Hoovels, P. Absil, and J. Van Campenhout, "Comparison of silicon ring modulators with interdigitated and lateral p-n junctions," *IEEE Journal on Selected Topics in Quantum Electronics*, vol. 19, no. 2, 2013.

[2] S. M. Leinders, W. J. Westerveld, J. Pozo, P. L. M. J. van Neer, B. Snyder, P. O'Brien, H. P. Urbach, N. de Jong, and M. D. Verweij, "A sensitive optical micro-machined ultrasound sensor (OMUS) based on a silicon photonic ring resonator on an acoustical membrane." *Scientific reports*, vol. 5, no. August, p. 14328, 2015.

[3] E. Hallynck and P. Bienstman, "Integrated optical pressure sensors in silicon-on-insulator," *IEEE Photonics Journal*, vol. 4, no. 2, pp. 443–450, 2012.

[4] N. A. Yebo, P. Lommens, Z. Hens, and R. Baets, "An integrated optic ethanol vapor sensor based on a silicon-on-insulator microring resonator coated with a porous ZnO film." *Optics express*, vol. 18, no. 11, pp. 11 859–66, 2010.

[5] C. F. Carlborg, K. B. Gylfason, a. Kaźmierczak, F. Dortu, M. J. Bañuls Polo, a. Maquieira Catala, G. M. Kresbach, H. Sohlström, T. Moh, L. Vivien, J. Popplewell, G. Ronan, C. a. Barrios, G. Stemme, and W. van der Wijngaart, "A packaged optical slot-waveguide ring resonator sensor array for multiplex label-free assays in labs-on-chips." *Lab on a chip*, vol. 10, no. 3, pp. 281–290, 2010.
[6] K. De Vos, J. Girones, T. Claes, Y. De Koninck, S. Popelka, E. Schacht, R. Baets, and P. Bienstman, "Multiplexed antibody detection with an array of silicon-on-insulator microring resonators," *IEEE Photonics Journal*, vol. 1, no. 4, pp. 225–235, 2009.
[7] A. Ramachandran, S. Wang, J. Clarke, S. J. Ja, D. Goad, L. Wald, E. M. Flood, E. Knobbe, J. V. Hryniewicz, S. T. Chu, D. Gill, W. Chen, O. King, and B. E. Little, "A universal biosensing platform based on optical micro-ring resonators," *Biosensors and Bioelectronics*, vol. 23, no. 7, pp. 939–944, 2008.
[8] M. Iqbal, M. A. Gleeson, B. Spaugh, F. Tybor, W. G. Gunn, M. Hochberg, T. Baehr-Jones, R. C. Bailey, and L. C. Gunn, "Label-free biosensor arrays based on silicon ring resonators and high-speed optical scanning instrumentation," *IEEE Journal on Selected Topics in Quantum Electronics*, vol. 16, no. 3, pp. 654–661, 2010.
[9] R. Heideman, M. Hoekman, and E. Schreuder, "TriPleX-based integrated optical ring resonators for lab-on-a-chip and environmental detection," *IEEE Journal on Selected Topics in Quantum Electronics*, vol. 18, no. 5, pp. 1583–1596, 2012.
[10] S. Chakravarty, W. C. Lai, Y. Zou, H. A. Drabkin, R. M. Gemmill, G. R. Simon, S. H. Chin, and R. T. Chen, "Multiplexed specific label-free detection of NCI-H358 lung cancer cell line lysates with silicon based photonic crystal microcavity biosensors," *Biosensors and Bioelectronics*, vol. 43, no. 1, pp. 50–55, 2013.
[11] A. Densmore, M. Vachon, D.-X. Xu, S. Janz, R. Ma, Y.-H. Li, G. Lopinski, A. Delâge, J. Lapointe, C. C. Luebbert, Q. Y. Liu, P. Cheben, and J. H. Schmid, "Silicon photonic wire biosensor array for multiplexed real-time and label-free molecular detection." *Optics letters*, vol. 34, no. 23, pp. 3598–3600, 2009.
[12] A. Ymeti, J. Greve, P. V. Lambeck, T. Wink, S. W. F. M. Van Novell, T. A. M. Beumer, R. R. Wijn, R. G. Heideman, V. Subramaniam, and J. S. Kanger, "Fast, ultrasensitive virus detection using a young interferometer sensor," *Nano Letters*, vol. 7, no. 2, pp. 394–397, 2007.
[13] S. Dante, D. Duval, B. Sepúlveda, A. B. González-Guerrero, J. R. Sendra, and L. M. Lechuga, "All-optical phase modulation for integrated interferometric biosensors," *Optics Express*, vol. 20, no. 7, p. 7195, 2012.
[14] B. J. Luff, J. S. Wilkinson, J. Piehler, U. Hollenbach, J. Ingenhoff, and N. Fabricius, "Integrated Optical Mach Zehnder Biosensor," *Journal of Lightwave Technology*, vol. 16, no. 4, pp. 583–592, 1998.
[15] P. Hua, B. Jonathan Luff, G. R. Quigley, J. S. Wilkinson, and K. Kawaguchi, "Integrated optical dual Mach-Zehnder interferometer sensor," *Sensors and Actuators, B: Chemical*, vol. 87, no. 2, pp. 250–257, 2002.
[16] E. Kleijn, E. van Vliet, D. Pustakhod, M. Smit, and X. Leijtens, "Amplitude and phase error correction algorithm for 3x3 MMI based Mach-Zehnder interferometers," *Journal of Lightwave Technology*, vol. 33, no. 11, pp. 2233–2239, 2015.
[17] "FIMMWAVE: A powerful waveguide mode solver," 2016. [Online]. Available: https://www.photond.com/products/fimmwave.htm
[18] A. Yariv, "Critical coupling and its control in optical waveguide-ring resonator systems," *IEEE Photonics Technology Letters*, vol. 14, no. 4, pp. 2001–2003, 2002.
[19] "ePIXfab: The silicon photonics platform."
[20] J. E. Saunders, C. Sanders, H. Chen, and H.-P. Loock, "Refractive indices of common solvents and solutions at 1550 nm," *Applied Optics*, vol. 55, no. 4, 2016.
[21] B. Snyder and P. O'Brien, "Packaging process for grating-coupled silicon photonic waveguides using angle-polished fibers," *IEEE Transactions on Components, Packaging and Manufacturing Technology*, vol. 3, no. 6, pp. 954–959, 2013.
[22] R. Halir, L. Vivien, X. Le Roux, D. X. Xu, and P. Cheben, "Direct and sensitive phase readout for integrated waveguide sensors," *IEEE Photonics Journal*, vol. 5, no. 4, 2013.

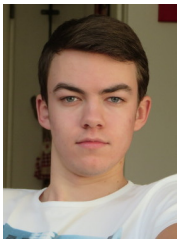

Ruben J. J. van Gulik is working towards his B.Sc degree in applied physics at the The Hague University of Applied Sciences.

In 2015, he completed an internship at the QuTech institute for quantum technology, where he developed software for data analysis.

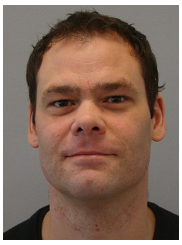

Bart M. de Boer received his Masters degree in electrical engineering from the Eindhoven University of Technology. In 2000 he joined Philips Research where he worked for ten years on various topics, such as integrated circuit design and signal processing for optical storage systems, magneto-resistive biosensors, biomedical instrumentation and finally on the Qi standard for wireless power transfer. In 2010 he joined TNO where, as a systems engineer, he has been involved in the development of sensors for space applications and photonic biosensors. Since 2014 he has coordinated the work on photonic biosensors at TNO.

Peter J. Harmsma received his MSc degree in applied physics at the University of Twente in 1993, and his PhD in 2000 at the University of Technology in Delft. From 2001 to 2005 he worked as R&D scientist at ThreeFive Photonics, of which he was one of the five founders. Subsequently, he joined ASML. Since 2008 he is a researcher at TNO, with main activities in integrated optics for (bio) sensors, metrology and spectroscopy. He has worked in InP, SOI and dielectric integrated optics platforms.